

Department of Physics and Astronomy
University of Heidelberg

Bachelor Thesis in Physics
submitted by

Christian Hensel

born in Mannheim (Germany)

2017

Zeeman-resolved spectroscopy of the coronal optical lines of Fe ions

This Bachelor Thesis has been carried out by Christian Hensel at the
Max-Planck-Institut für Kernphysik in Heidelberg
under the supervision of
Priv.-Doz. Dr. José Ramón Crespo López-Urrutia

Abstract

Zeeman-resolved spectroscopy of the coronal optical lines of Fe ions

In this work, the following transitions are spectroscopically investigated: Fe^{13+} at 530 nm, Fe^{9+} at 637 nm, Fe^{12+} at 339 nm and Fe^{10+} at 789 nm. These transitions occur in the solar corona and other stars and are therefore of astrophysical interest. Reference wavelength values are needed to determine plasma movements and temperatures in those stars, but scarce laboratory measurements are available and theoretical calculations are not sufficiently precise. In our case, those highly charged ions are produced in the laboratory using an electron beam ion trap. The wavelengths and g -factors are determined: 530.42870(8) nm, 637.6277(4) nm, 338.8930(3) nm, 789.3915(8) nm. For the Fe^{13+} at 530 nm, Fe^{9+} at 637 nm and Fe^{10+} at 789 nm transitions, the Zeeman components are well resolved. For all the measured wavelength, the uncertainty is 5-14 times smaller than for the previous best measurement.

Zeeman-auflösende Spektroskopie der koronalen optischen Linien von Fe Ionen

In dieser Arbeit werden die folgenden Übergänge spektroskopisch untersucht: Fe^{13+} bei 530 nm, Fe^{9+} bei 637 nm, Fe^{12+} bei 339 nm und Fe^{10+} bei 789 nm. Diese Übergänge finden in der Korona der Sonne und anderer Sterne statt und sind somit von astrophysikalischem Interesse. Referenz-Wellenlängen werden benötigt um Plasma-Bewegungen und -Temperaturen zu bestimmen, aber wenige Labormessungen sind verfügbar und theoretische Berechnungen erreichen noch keine ausreichende Genauigkeit. Diese hochgeladenen Ionen wurden im Labor durch eine Elektronenstrahl-Ionenfalle produziert und gefangen. Die Wellenlängen und g -Faktoren wurden bestimmt: 530.42870(8) nm, 637.6277(4) nm, 338.8930(3) nm, 789.3915(8) nm. Für die Fe^{13+} bei 530 nm, Fe^{9+} bei 637 nm und Fe^{10+} bei 789 nm Linien sind die Zeeman-Komponenten gut aufgelöst. Für alle gemessenen Wellenlängen ist die Genauigkeit um 5 bis 14 mal besser als die vorherige beste Messung.

Contents

1	Introduction	1
2	Theory	5
2.1	Hydrogen-like quantum systems	5
2.2	Spin-orbit interaction and fine structure	6
2.2.1	Magnetic moment	6
2.2.2	Fine structure	8
2.3	Zeeman effect	10
2.3.1	Zeeman effect in a weak field	10
2.4	Electron transitions	12
2.4.1	Selection rules	12
2.4.2	Polarization of emitted radiation	13
2.4.3	Branching ratio of transitions	14
2.5	Line width	15
2.5.1	Natural line width	15
2.5.2	Doppler broadening	16
3	Experiment	19
3.1	Electron beam ion trap (EBIT)	19
3.1.1	Principle	19
3.1.2	Heidelberg EBIT	21
3.2	Optical setup	23
3.2.1	Optical path EBIT to Spectrometer	23
3.2.2	Spectrometer	24
3.2.3	CCD	26
3.2.4	Polariser	27
3.3	Measurement	30
3.3.1	Adjusting the EBIT	30

3.3.2	Adjusting the optical setup	31
3.3.3	Measuring procedure	32
4	Analysis and Results	33
4.1	Processing of the Spectra	33
4.2	Calibration procedure	34
4.3	Zeeman fitting model	38
4.4	Uncertainty of the counts	39
4.5	Measured spectral lines of Fe ions	40
4.5.1	Fe ¹³⁺ at 530 nm	40
4.5.2	Fe ⁹⁺ at 637 nm	44
4.5.3	Fe ¹²⁺ at 339 nm	48
4.5.4	Fe ¹⁰⁺ at 789 nm	53
4.5.5	Fe ¹⁴⁺ at 706 nm	57
4.6	Ion cloud temperature	57
4.7	Polarisation	58
4.8	Magnetic field in the EBIT	60
4.9	Wavelength corrections of the solar observations	61
4.9.1	Transversal Doppler Effect	61
4.9.2	Gravitational redshift	62
5	Discussion	63
	Bibliography	73

Chapter 1

Introduction

Newton was one of the first to discover that the white light of the sun can be dispersed into a range of colours by using a prism [1]. In 1814, Fraunhofer observed dark lines in the sun's spectrum [2]. This work initiated the growing importance of spectroscopy in science. Kirchhoff and Bunsen discovered in 1860 at Heidelberg, that every element has characteristic absorption wavelengths [3], which also caused the lines observed by Fraunhofer. On this way, the composition of the solar surface could be determined.

During a total solar eclipse in 1869, Harkness and Young discovered a green emission line in the coronal spectrum [4]. The corona (lat. crown) is the region of hot plasma surrounding the sun and other stars. The corona of the sun is millions of kilometres thick and is the source of the solar wind that strongly affects the upper atmosphere of the earth. The observed green line could not be assigned to any known element and therefore, the theory of a new element called Coronium arose. In 1939, Grotian and Edlén theoretically calculated the transition energies of highly charged ions (HCI) and the green line was identified as a Fe^{13+} transition [5]. Also, other lines of the corona were assigned to highly charged Fe ions. The production of HCI requires high energies which led to the corona temperature to be of millions of Kelvin [6], compared to 5800 Kelvin of the solar surface. The energy transport processes of solar surface and corona are still not completely understood and is a field of ongoing research.

Iron is the most common heavy element in the universe and appears as HCI in stars. The wavelengths determined in the laboratory are used in astronomy to calculate plasma temperatures and other proprieties which relate to a reference wavelength (rest frame) like the Doppler effect. Even advanced theory cannot predict the wavelengths with sufficient precision, due to the large effort of the numerical calculations, which are limited by the available computational possibilities. For the Fe^{13+} at 530 nm line, multiple theoretical models have been calculated. The recent work by Schnorr [7] has 0.5 nm uncertainty on the wavelength.

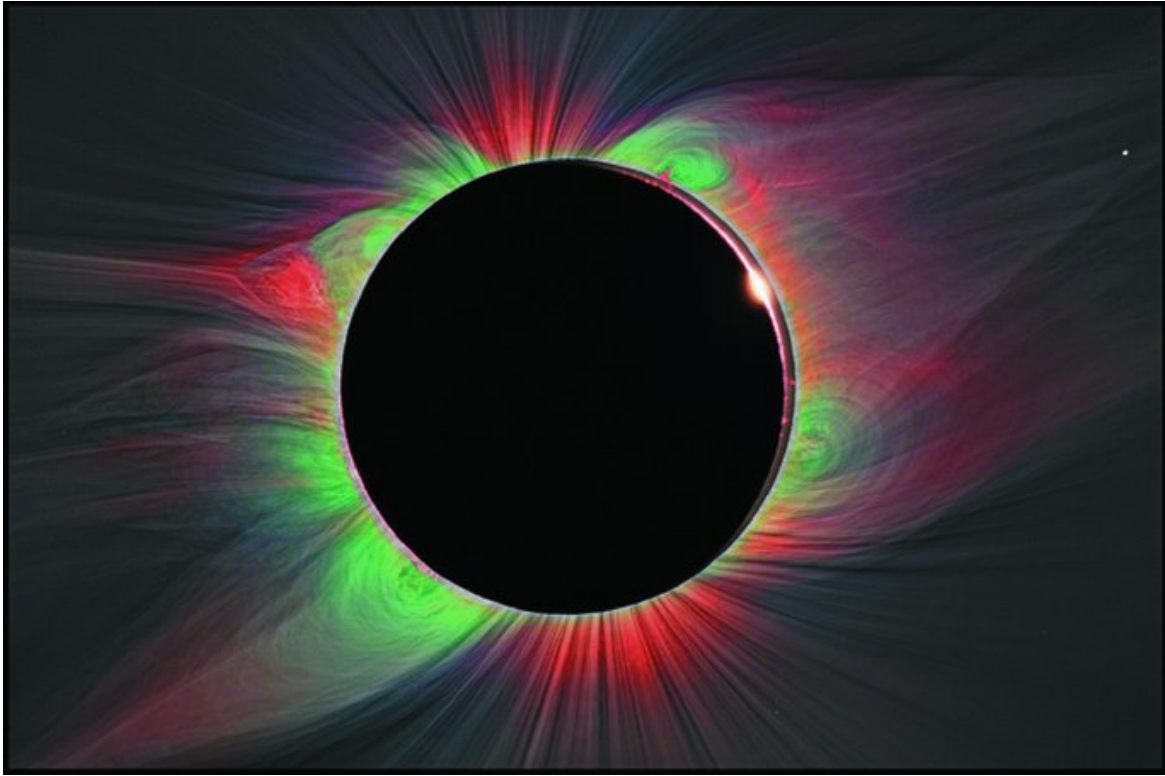


Figure 1.1 Overlay of the emissions from $\text{Fe}^{9+} / \text{Fe}^{10+}$ in red and $\text{Fe}^{12+} / \text{Fe}^{13+}$ in green. The fine structures are from an underlying white image [8]. Except from the Fe^{12+} line, the observed wavelength are determined in this work.

Only scarce laboratory measurements are available for these transitions. The objective is to obtain more precise values for the wavelength to improve precision in astronomical analysis.

In this work, the transitions of Fe^{13+} at 530 nm, the stated green line, Fe^{9+} at 637 nm, Fe^{12+} at 339 nm and Fe^{10+} at 789 nm are investigated. In works of Habbal 2010 [8] these Fe^{13+} , Fe^{9+} and Fe^{10+} lines are observed in the solar corona, visualised in figure 1.1. These HCI are sources of radiation all over the universe, e.g. the Fe^{13+} at 530 nm transition was observed in spiral galaxies [9], remains of a supernova [10] and red dwarfs [11]. The Fe^{13+} and Fe^{9+} are prominent in the spectrum of the 5000 light years distant nova system RS Ophiuchi (figure 1.2), which is of special astrophysical interest because it is a binary system of white dwarf and red giant [12].

In this work an electron beam ion trap (EBIT) is used to produce and trap the Fe ions. The electron beam is used to ionize, radially trap and excite the ions. Using two superconducting coils, a magnetic field applies an axial trapping potential. This device is capable of precisely producing charged states for almost any atoms and is easily accessible for an optical spectrometer. For high precision measurements, a Doppler shift is avoided, due to the symmetry of the ion movement. Because of relatively low plasma density, relaxation of the states due to ion-ion collision is strongly suppressed and therefore the EBIT resembles the condition of the coronal plasma, where also the natural decay is the main source of the radiation. Due to the strong nuclear field of HCI, the influence of trapping potentials on transitions are relatively small. For theory, HCI are also interesting because of the dynamics of single or few electron systems are relatively easy to predict. However, for these ions the theoretical models are not sufficiently precise yet and new models need accurate data to be tested.

Chapter 2

Theory

2.1 Hydrogen-like quantum systems

When first stepping into quantum mechanics, the hydrogen atom is a relatively simple model to consider, because it consists only of two bodies (a proton and an electron). For such a system, the Schrödinger equation 2.1, which describes the state of a quantum system over time, can be solved analytically.

$$H \psi(\vec{r}, t) = i \frac{\partial}{\partial t} \psi(\vec{r}, t) \quad (2.1)$$

$\psi(\vec{r}, t)$ is the wave function of the system representing its state and H the Hamiltonian. This H operator is describing the total energy of a particle of mass m in the potential $V(\vec{r}, t)$, given by

$$H = -\frac{\hbar^2}{2m} \vec{\Delta} + V(\vec{r}, t). \quad (2.2)$$

where \hbar is the reduced Planck constant and m the mass of the particle. In the time independent case, where V only depends on \vec{r} , the separation ansatz $\psi(\vec{r}, t) = R(r) \cdot Y(\theta, \phi)$ is used to solve the Schrödinger equation.

Atoms with only one electron are called hydrogen-like, because they only differ from the nucleus charge of the hydrogen atom and can be approximated to two body systems. In this case, the non-relativistic first-order approximation can be described as a system of two point particles with a Z times charged nuclei and one electron e . Using the Coulomb potential at a distance r from the nucleus given by $V(r) = -\frac{Ze^2}{4\pi\epsilon_0 r}$, the resulting energy eigenvalues E_n of

the atom are

$$E_n = -\frac{m Z^2 e^2}{32(\pi \epsilon_0 n)^2} \quad (2.3)$$

where n the principal quantum number and ϵ_0 the vacuum permittivity.

2.2 Spin-orbit interaction and fine structure

following the derivation of Haken [13]

In a spectrum, the energy states are observed as lines of a certain wavelength. With increasing resolution of atomic spectroscopy, a splitting of the lines was discovered in the Na D line [14]. These phenomena were observed in all atoms with one valence electron and non-zero angular momenta. Therefore, it cannot be explained with the electron — electron interaction. In 1922 Stern and Gerlach discovered that the electron itself has a property which can be interpreted as an angular momentum and was called the spin [15]. To understand this doublet structure a further understanding of the magnetic moments of the angular momentum μ_l , of the spin μ_s needed. The interaction of momenta and spins of the electrons lead to the substructure of energy levels, called fine structure.

2.2.1 Magnetic moment

The magnetic moment of an electron in an atom leads to different modes of oscillation which corresponds to different energies. This magnetic moment consists of orbital and spin components.

Orbital angular momentum

The magnetic moment of the electron on a circular orbit is given by

$$\vec{\mu}_l = -\frac{e}{2m_0} \vec{l} \quad (2.4)$$

with $|\vec{l}| = m_0 \omega r^2$. Where \vec{l} is the angular momentum of the electron, ω the frequency of orbital circulations, r the distance of the electron to the nucleus, m_0 the rest mass of the electron and e its charge. The magnetic moment of an electron with angular momentum

$|\vec{l}| = \hbar$, with \hbar as the reduced Plank constant, is called Bohr magneton μ_B and is given by:

$$\mu_B = \frac{e}{2m_0}\hbar = 9.274078 \cdot 10^{-24}(\text{Am})^2 \quad (2.5)$$

μ_B is used as a unit of angular momentum in atomic physics. Thus, the magnetic moment of the orbital angular momentum is

$$\vec{\mu}_l = -g_l \mu_B \frac{\vec{l}}{\hbar} \quad (2.6)$$

The factor g_l is called 'g-factor' and depends on the atom configuration. In section 2.3, the characteristics of the g-factor will be discussed in more detail, and will be calculated using the Landé equation.

Spin

Even $l=0$, atoms have a magnetic moment due to their intrinsic electron spin. This leads to the energy deviation of the duplet lines found in atomic spectra. The magnetic moment of the electron is

$$\vec{\mu}_s = -g_s \frac{e}{2m_0} \vec{s} \quad (2.7)$$

With g_s as the g-factor of the spin, and \vec{s} as the spin vector of the electron.

2.2.2 Fine structure

The fine structure is due to the magnetic interaction of orbital and intrinsic (spin) angular momenta of the electrons. The combination of them leads to the total angular momentum \vec{j} with the absolute value of $j = |l \pm 1/2|$ for the here discussed $s = 1/2$ systems.

In the reference frame, in which the electron does not move but the nucleus performs a circular movement, according to the Biot-Savart's law, the magnetic field is

$$\vec{B}_l = \frac{Ze\mu_0}{4\pi r^3}(\vec{v} \times \vec{r}) = \frac{Ze\mu_0}{4\pi r^3 m_0} \vec{l} \quad (2.8)$$

where $\vec{l} = \vec{r} \times (m_0 \vec{v})$, \vec{v} the velocity vector and μ_0 the vacuum permeability.

The spin \vec{s} and $\vec{\mu}_s$ precesses around the emerging magnetic field of the orbital angular momentum \vec{B}_l (figure 2.1).

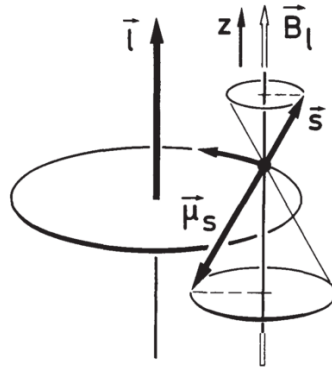


Figure 2.1 Precession of the spin around the magnetic field B_l with the quantized components of s_z and $\mu_{s,z}$ as the projection of \vec{s} and $\vec{\mu}_s$ on the z-axis. [13]

The interaction energy of spin and orbital-angular-momentum, using the spin magnetic moment (2.7) and the magnetic field (2.8), is

$$V_{s,l} = -\vec{\mu}_s \cdot \vec{B}_l = \frac{Ze^2 \mu_0}{8\pi m_0^2 r^3} (\vec{s} \cdot \vec{l}). \quad (2.9)$$

We can express this also in terms of quantum numbers j, s, l

$$V_{s,l} = -\frac{a}{\hbar^2} |\vec{l}| \cdot |\vec{s}| \cos \angle(\vec{l}, \vec{s}) \quad (2.10)$$

$$= \frac{a}{2} (j(j+1) - l(l+1) - s(s+1)) \quad (2.11)$$

with $\angle(\vec{l}, \vec{s})$ as the angle between those vectors and the spin-orbit coupling constant a defined as

$$a = \frac{Ze^2 \mu_0 \hbar^2}{8\pi m_0^2 r^3} \quad (2.12)$$

The total energy of a fine split state can be obtained by

$$E_{n,l,j} = E_{n,l} + E_{l,s} + E_{rel} \quad (2.13)$$

where $E_{n,l}$ is the eigenstate energy in the hydrogen-like case (2.3), $E_{l,s}$ is the just derived fine structure interaction energy 2.10 and E_{rel} is a relativistic correction term according to Dirac but not calculated here. The result is

$$E_{FS} = -\frac{E_n \alpha^2}{n} \left(\frac{1}{j+1/2} - \frac{3}{4n} \right) \cdot Z^2 \quad (2.14)$$

with the fine structure constant

$$\alpha = \frac{e^2}{4\pi\epsilon_0 \hbar c} \approx \frac{1}{137}. \quad (2.15)$$

2.3 Zeeman effect

When the atom is in an external magnetic field, multiple splittings in the spectral lines occur due to the Zeeman effect.

2.3.1 Zeeman effect in a weak field

following the derivation of Foot [16]

The vectorial sum of the orbital angular momentum \vec{l} and the intrinsic \vec{s} results in the total angular momentum \vec{j} with the length $|\vec{j}| = \sqrt{j(j+1)}\hbar$. This quantity is conserved in case the spin orbit interaction dominates over the effect of the external magnetic field. In case of highly charged ions, this is most of the times the case due to the strong fields inside the ion. However, the individual quantities \vec{l} and \vec{s} are not separately conserved.

Under the influence of the external magnetic field in z direction \vec{B}_z , the total angular momentum \vec{j} performs a precession movement around the z axes. The interaction of \vec{l} and \vec{s} leads to their precession and results in the precession of the total magnetic moment μ around the \vec{j} axis (figure 2.2), described by

$$\vec{\mu} = \vec{\mu}_s + \vec{\mu}_l = -\mu_B \cdot \frac{g_l \vec{l} + g_s \vec{s}}{\hbar} \quad (2.16)$$

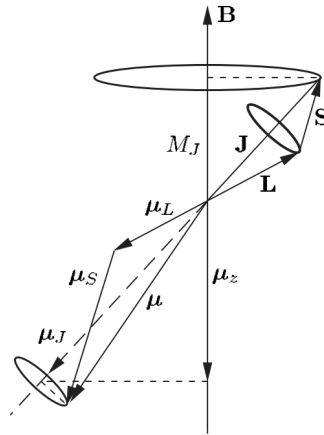


Figure 2.2 The orbital motion and the spin are projected along \vec{j} and contribute to the total magnetic moment μ_j . [16]

The Hamiltonian of the Zeeman effect H_{ZE} is

$$H_{ZE} = -\vec{\mu}\vec{B} \quad (2.17)$$

with $\vec{B} = B\vec{e}_z$ the Hamilton operator is

$$H_{ZE} = -\frac{\langle\vec{\mu}\cdot\vec{j}\rangle}{j(j+1)}\vec{j}\cdot\vec{B} = \frac{\langle\vec{l}\cdot\vec{j}\rangle + g_s\langle\vec{s}\cdot\vec{j}\rangle}{j(j+1)}\frac{\mu_B}{\hbar}Bj_z \quad (2.18)$$

The first term is the Landé- g -factor g_j . In the vector model, the brackets are the time averages. To calculate the time average of the total magnetic moment $\vec{\mu}$, the time averages of the separate angular momenta are used, which result in their projection on \vec{j} .

$$\langle\vec{s}\cdot\vec{j}\rangle = \frac{1}{2}(\vec{j}^2 + \vec{s}^2 - \vec{l}^2) = \frac{\hbar^2}{2}(j(j+1) + s(s+1) - l(l+1)) \quad (2.19)$$

$$\langle\vec{l}\cdot\vec{j}\rangle = \frac{1}{2}(\vec{j}^2 - \vec{s}^2 + \vec{l}^2) = \frac{\hbar^2}{2}(j(j+1) - s(s+1) + l(l+1)) \quad (2.20)$$

with $g_s = 2$, the Landé- g -factor therefore, is

$$g_j = \frac{3}{2} + \frac{s(s+1) - l(l+1)}{2j(j+1)} \quad (2.21)$$

The total energy difference due to the Zeeman effect is

$$E_{ZE} = g_j \mu_B B m_j \quad (2.22)$$

Where the projection of the total angular momentum on the z axes is given by $j_z = m_j \hbar$, using the magnetic quantum number of the total angular momentum $-j \leq m_j \leq +j$.

Due to historical reasons, we distinguish between normal and anomalous Zeeman effect. The normal case, i.e. for $s = 0$, leads to $g_j = 1$ and an energy split independent of the total angular momentum \vec{j} . In the anomalous case, when $s \neq 0$, the g_j values vary.

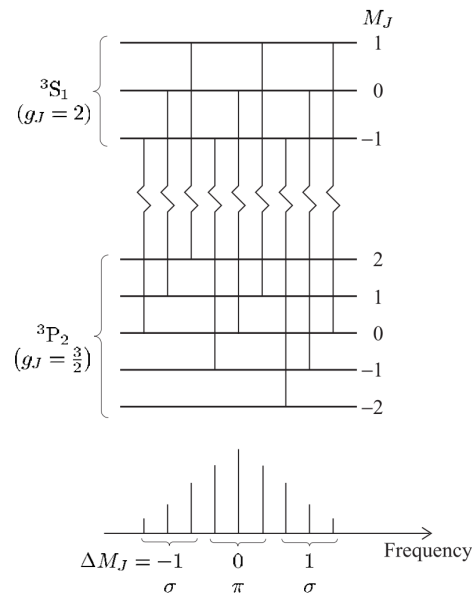


Figure 2.3 The anomalous Zeeman effect of the $6s6p3P_2 - 6s7s3S_1$ transition in mercury. The levels have different g_j values due to different s values. [16]

2.4 Electron transitions

An atomic electron transition is the energy level change of an electron in the atom. In this work, however, we will just discuss the ones in which the electrons change from a higher to a lower energy state, in which the energy difference is emitted in the form of an electromagnetic wave.

2.4.1 Selection rules

Transitions have a very much different rate depending on the initial and final state. Using perturbation theory of the states influenced by an electric field Fermi's golden rule¹ can be derived, which gives the rate of transition from the initial state $\langle i|$ to the final state $\langle f|$:

$$\Gamma_{i \rightarrow f} = \frac{2\pi}{\hbar} \rho_f |\langle f|V|i\rangle|^2 \quad (2.23)$$

¹This was initially done by Paul Dirac in 1927 [17] but Fermi dubbed it 'golden rule' due to its importance in atomic physics [18].

where V is the perturbation part of the Hamiltonian, ρ_f the density of final states and $\langle f|V|i\rangle$ the probability of a transition given by the 'matrix element' [19]. Many of these transition probabilities $\langle f|V|i\rangle$ are zero, due to the symmetry properties of the wave functions in these states. For configurations of initial and final state for which this matrix element is non-zero, the selection rules can be formulated 2.1.

Table 2.1 For the hydrogen-like systems the transition rules for magnetic and electronic dipole transitions are formulated in terms of quantum numbers for discrete transitions given in [20]

dipole moment		quadrupole moment
electronic	magnetic	electronic
E1	M1	E2
$\Delta J = 0, \pm 1$ (except $0 \leftrightarrow 0$)	$\Delta J = 0, \pm 1$ (except $0 \leftrightarrow 0$)	$\Delta J = 0, \pm 1, \pm 2$ (except $0 \leftrightarrow 0,$ $1/2 \leftrightarrow 1/2, 0 \leftrightarrow 1$)
$\Delta M = 0, \pm 1$ (except $0 \leftrightarrow 0$ when $\Delta J = 0$)	$\Delta M = 0, \pm 1$ (except $0 \leftrightarrow 0$ when $\Delta J = 0$)	$\Delta M = 0, \pm 1, \pm 2$
parity change	no parity change	no parity change
$\Delta l = \pm 1$	$\Delta l = 0$	$\Delta l = 0, \pm 2$
Δn arbitrary	$\Delta n = 0$	Δn arbitrary

2.4.2 Polarization of emitted radiation

The polarisation of the emitted radiation can be derived by the orientation of the total angular momentum of the states m_j involved in the Zeeman transition. Looking at table 2.1, for an E1 transition and a z-orientated magnetic field, the polarisations on the x-y observation plane result in two perpendicular polarisations (figure 2.4a, 2.4b). For $\Delta m_j = \pm 1$ the dipole moments along the x-axis are non-zero and of opposite sign. Both $\Delta m_j = \pm 1$ polarisations are phase-shifted by π and called $\pm\sigma$. For $\Delta m_j = 0$, the charge oscillates parallel to the magnetic field, along the z-axis, and emits linearly polarised radiation in x and y. This polarisation is called π . For $\Delta m_j > 1$ no E1 transition is possible according to the selection rules.

For magnetic dipole transitions it is the other way around: for $\Delta m_j = 0$ the π -transitions and for $\Delta m_j = \pm 1$ the σ -transitions.

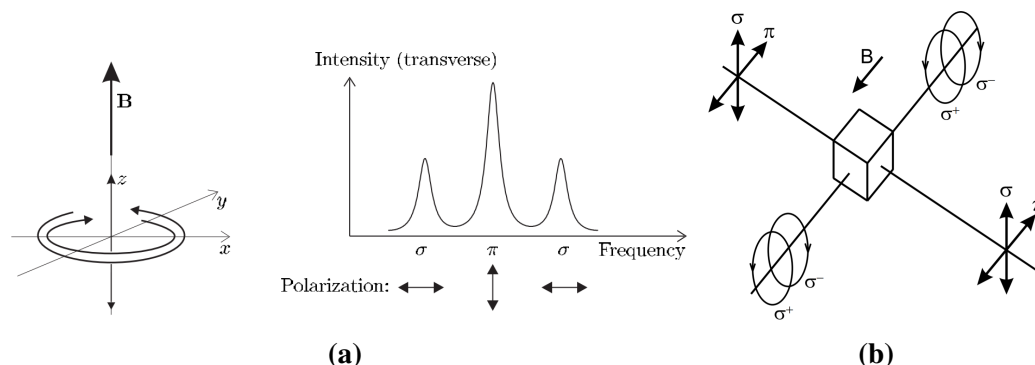


Figure 2.4 (a) For the Zeeman effect the polarisations of the line components (left side) originates in the orientation of the oscillation modes in the magnetic field B (right side). [16] (b) The observed polarisations depend on the axis of observation relative to the magnetic field and the axis of observation. [21]

The probability for a M1 transition is typically 2-3 orders of magnitude lower than an E1 dipole transition [22]. The quadrupole transitions are multiple orders of magnitude smaller than the dipole transitions. For example, with a magnetic moment of two Bohr radii, at 500 nm the E2 transition is eight orders of magnitude smaller than of E1 [22]. Nevertheless, these transitions are possible and can be observed in highly charged ions where the magnetic moments are large. In this work, these transitions give all the measured Fe lines.

2.4.3 Branching ratio of transitions

The branching ratios of the transitions between two quantum mechanical states are given by the Clebsch-Gordan coefficients (CGC). This can be derived using the Wigner-Eckart theorem on the angular momentum operator in the basis of its eigenstates. This theorem states that the matrix element of the transition can be expressed using two factors, one of which being the CGC. In a mathematical sense, the Clebsch-Gordan coefficients are the expansion coefficients of the total angular momentum operator in an uncoupled basis. So, they are used for coupled states of the two angular momenta.

Calculating these coefficients is an advanced quantum mechanical task but tables for these coefficients are available. The CGC lead to the branching ratio of the different Zeeman transitions.

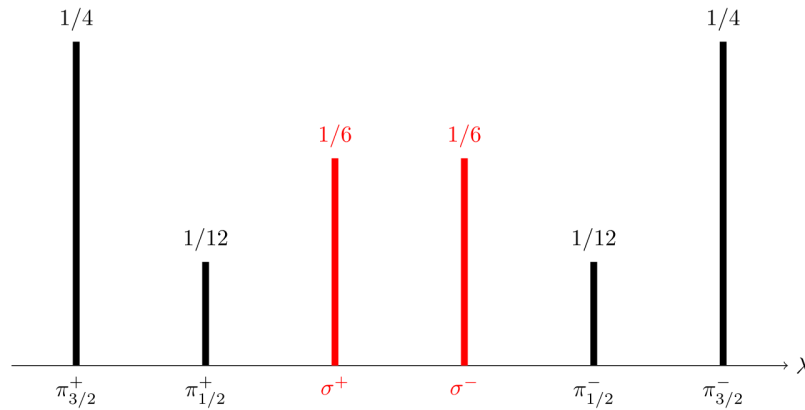


Figure 2.5 Branching ratio of the $Fe^{13+} 2P_{1/2} \rightarrow 2P_{3/2}$ transition, calculated using CGC in [23]. The lines are labelled with $\pi_{3/2}^{\pm}$ for the π -polarised line from the initial state with $m_j = \pm 3/2$ (analogue for $1/2$).

2.5 Line width

In spectroscopy, the uncertainty of measured transition energies of the different states relates to the line profile and width of the spectral line. Therefore, the effects of how the in principle discrete energy of this transition results in a non-discrete line shape, observable in the spectrum, need to be considered.

2.5.1 Natural line width

following the derivation of Haken [13]

The line width is not completely discrete due to the Heisenberg uncertainty principle.

$$\Delta E \cdot \Delta t > \frac{\hbar}{2} \quad (2.24)$$

The line widths of the spectral lines are given by the lifetimes of the energy states which lead to the transition. To have an idea of how the full width at half maximum (FWHM) relates to the lifetime of the excited state without doing the derivation, first the population of a state needs to be considered. The number of atoms in a certain excited state reduces over time by an exponential decay:

$$N = N_0 \exp(-2\gamma t) \quad (2.25)$$

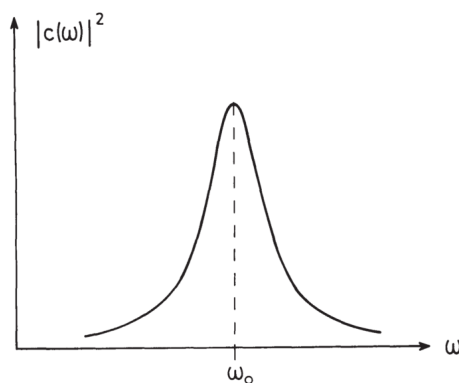


Figure 2.6 Lorentz profile with the natural line width of the spectral line. [13]

with $t_0 = 1/(2\gamma)$ being the time in which the number N decayed to the e -th part of the initial value and is called the lifetime of the state. The amplitude of the radiational field is given by

$$F(t) = F_0(\exp(-\gamma t) \exp(i\omega_0 t + c.c.)) \quad (2.26)$$

with the centre frequency of this transition $\omega_0 = (E_i - E_f)/\hbar$. Using a Fourier transformation, which is not done here, will lead to the intensity distribution $c(\omega)$ of monochromatic light at frequency ω .

$$|c(\omega)|^2 = F_0^2 \frac{1}{(\omega - \omega_0)^2 + \gamma^2} \quad (2.27)$$

The natural line width is $\gamma = 1/(2t_0)$.

2.5.2 Doppler broadening

following the derivations of Haken and Foot [13, 16]

The movements of the ions, relative to the observer, in the hot ion cloud influences the line width due to the Doppler effect. The shifted frequency ω is given by

$$\omega = \omega_0 - kv \quad (2.28)$$

with ω_0 the frequency in the atoms rest frame and the wave vector's absolute value $k = \omega_0/c = 2\pi/\lambda$, $\vec{k} \cdot \vec{v} = kv$ with \vec{v} the velocity of the atom in the rest frame of the wave. Moving atoms absorb radiation with a frequency shift of $\delta = \omega - \omega_0 = kv$ which leads to the relative frequency shift of

$$\frac{\delta}{\omega_0} = \frac{v}{c} \quad (2.29)$$

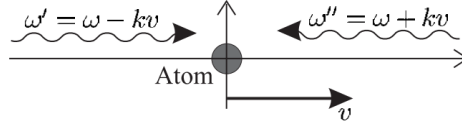


Figure 2.7 Doppler effect for the observed frequencies. In the laboratory system, the radiation has the frequency ω and in a moving system the shown frequencies. Only the k component of the movement contributes to the frequency shift. [16]

We look at the Maxwell distributed velocities, in the interval from v to $v + dv$,

$$f(v)dv = \sqrt{\frac{M}{2\pi k_B T}} \exp\left(-\frac{Mv^2}{2k_B T}\right) dv \quad (2.30)$$

with the atomic mass M , the temperature T and the Boltzmann constant k_B . Using (2.29) which relates velocity shift with frequency, the Gaussian shaped line profile is

$$I(\omega) = const \cdot \exp\left(-\frac{Mc^2(\omega - \omega_0)^2}{2k_B T \omega_0^2}\right) \quad (2.31)$$

This line profiles FWHM is

$$\Delta\omega = \frac{\omega_0}{c} \sqrt{8 \ln 2 k_B T / M} \quad (2.32)$$

Chapter 3

Experiment

In order to determine the wavelength of the Fe lines, the highly charged states need to be produced and trapped. This is done using an electron beam ion trap (EBIT) because it is a rather simple and energy efficient way to produce different highly charged ions (HCI). The spectrum is measured using a Czerny-Turner monochromator and a CCD.

This chapter follows the path of the radiation from EBIT to monochromator and CCD before stating the used experimental parameters and procedures.

3.1 Electron beam ion trap (EBIT)

3.1.1 Principle

The electron gun accelerates the electrons through the drift tubes, across the trap centre, where an axial trapping potential is applied. In this region, the neutral atoms are injected and ionized by electron impact ionisation. Subsequently, the electrons are dumped in the collector (see figure 3.1).

The electron beam is used both for ionisation, and radial confinement, due to the Coulomb potential of the ions. Also, the emission of photons from the ions in the trap centre are due to their excitations from electron impact processes.

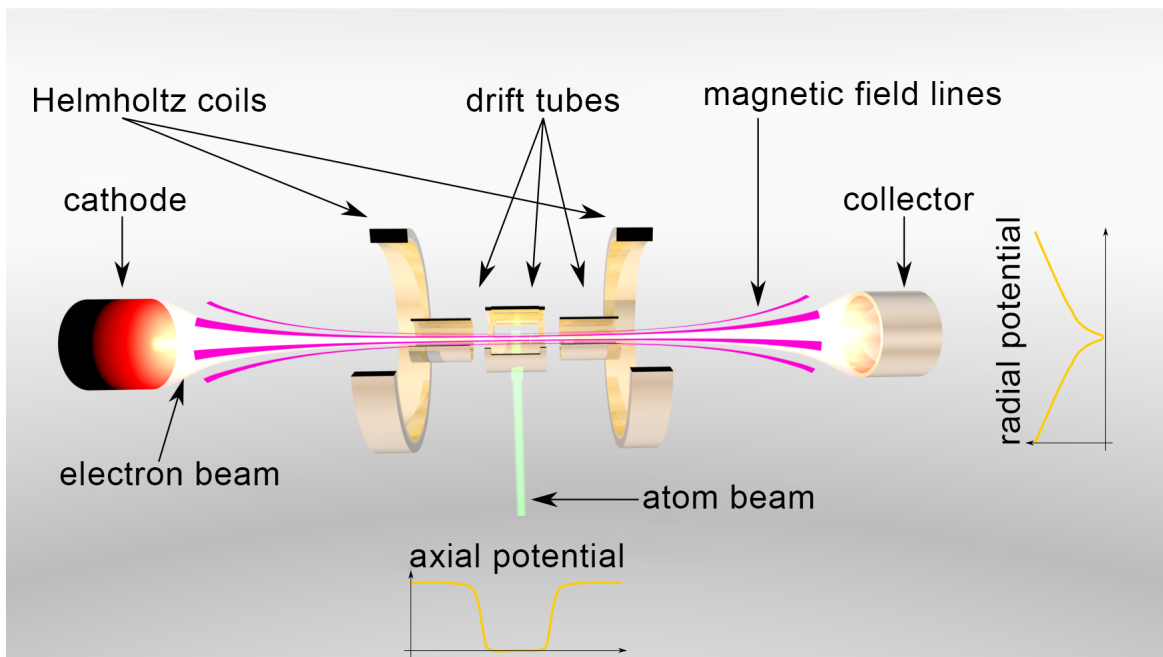


Figure 3.1 The working principle of the EBIT. The electron beam (white) is emitted from the cathode (left), is compressed by the magnetic field (purple lines) of the coils and broadened towards the collector on the right where the beam is absorbed. The drift tubes form the trapping potential in axial direction (bottom). ([24] modified)

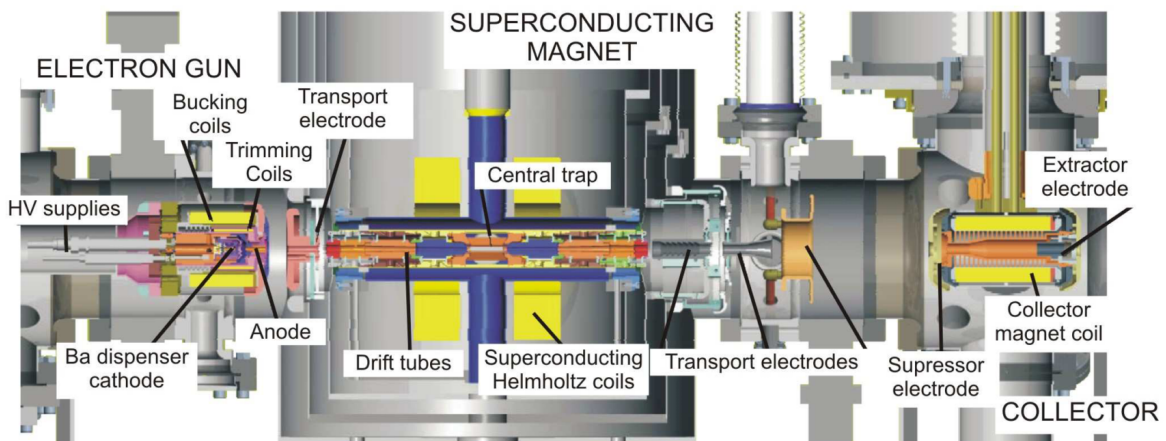


Figure 3.2 Cross section of the HD-EBIT with the electron gun (left), the trapping region (middle) and the collector (right). The superconducting magnets are shielded by multiple layers of cooled confinements. [25]

3.1.2 Heidelberg EBIT

In this work, the EBIT named Heidelberg (HD-EBIT) was used (figure 3.2). This section is following the path of the electrons in the trap.

In the electron gun, a barium-wolfram cathode emits electrons due to the thermionic effect. When heating the cathode, also barium and wolfram atoms are emitted and contaminate the trap. To prevent this, the trapping potential is inverted regularly, in a process called dumping. The electrons are accelerated by the potential gradient between the cathode and the anode. For a collimated beam, a coil around the gun compensates the magnetic field created by the superconducting Helmholtz coils.

The electrons are passing through the trapping region, which is split up into segments that apply an electric field on the ions. In the Heidelberg EBIT, nine of those segments, called drift tubes, are individually adjusted to create an optimal potential for each ion charge state and mass. At the centre, the electron beam is compressed radially to a diameter of about 50 μm by two superconducting coils in Helmholtz configuration. The coils, at close to 4 K, create a magnetic flux density of approximately 8 T. At the central drift tube, four axial slits open the ion cloud region for detectors and the atom injection system. From the bottom slit $\text{Fe}(\text{CO})_5$ is injected as it is volatile at room temperature. The electron beam easily brakes the molecular bonds and the light elements C and O enhance evaporative cooling, which result in a smaller Doppler broadening. The atoms are ionised by electron impact processes and in the decay of excited states photons are emitted. When using optical spectroscopy, two quartz lenses lead the light to a quartz window (figure 3.3) and to the further optical setup (section 3.2.1).

Behind the trapping region, the electrons are dumped in the collector. A magnetic field diverges the electron beam strongly and directs it towards a water cooled inner tube, what prevents the electrons of reflecting back into the trapping region. The collector is directly connected to the cathode, so the electrical circuit is closed. In case an electron passes the whole way through that field an additional electrode stops it at a more negative potential than the cathode. The whole described setup is under high vacuum with pressures of about 10^{-10} mbar for magnet, gun and collector and of $10^{-9} - 10^{-7}$ mbar for beam line and injection system.

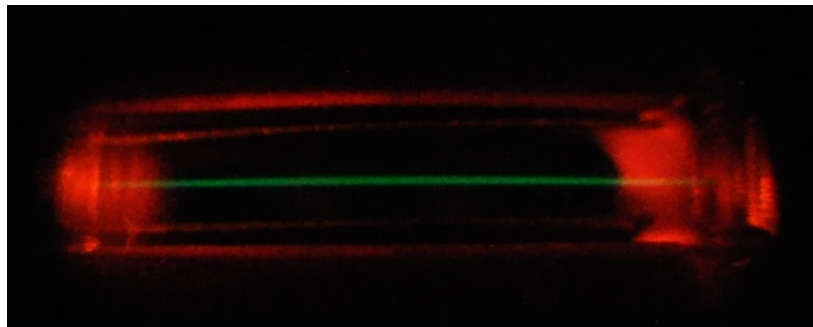


Figure 3.3 Photograph of the Fe¹³⁺ ion cloud in the trap centre. The red light are reflections of the cathode on the drift tubes. [26, 27]

The electron beam energy is estimated as the potential difference between cathode and central drift tube:

$$E_e = e(-U_{\text{cathode}} + U_{\text{centre drift tube}}). \quad (3.1)$$

This equation does not take the effect of the space charge of ions and electrons into account. The charge of the compressed electron beam contributes to the potential present at the trapping region. This is the reason why the electron beam energy needs to be set to a higher value than the ionisation energy of the atom.

For lower trapping potentials, evaporative cooling is enhanced, as only the lowest energy atoms of the charged states remain in the trap. Particles with higher kinetic energies leave the trap.

3.2 Optical setup

Since the to be measured Fe lines are in the optical range, an optical spectrometer is used to determine the wavelength distribution. The light beam is guided from the trapping region to the monochromator, where the spectral components are separated using a diffraction grating, and finally detected and accumulated by a CCD camera (figure 3.4).

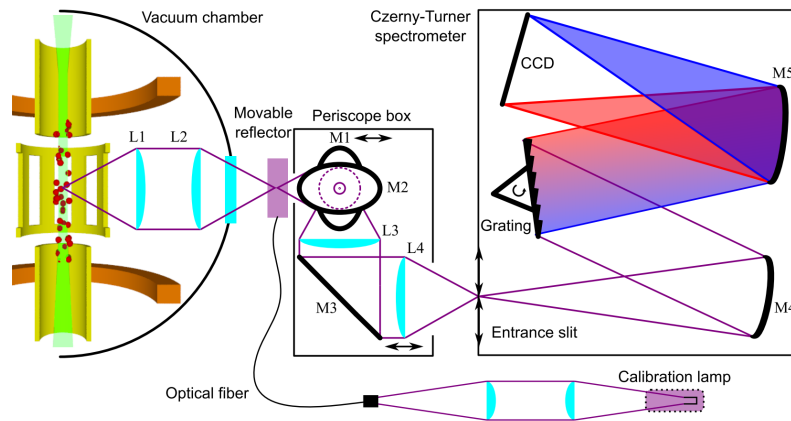


Figure 3.4 Schematics of the optical setup including image rotation system ('periscope box'), spectrometer (right) and calibration lamp (bottom). The EBIT, including the lenses inside the vacuum, is on the left. Elements which are adjusted in this work are indicated by arrows. In contrast to this figure, the light is guided to the CCD with an additional mirror. [28, 29]

3.2.1 Optical path EBIT to Spectrometer

Inside the vacuum region of the EBIT, two lenses focus the light on the quartz window. Since the ion cloud in the EBIT is horizontally expanded, the emitted light needs to be rotated before entering the spectrometer's vertical slit. This rotation is performed by two mirrors (a,b in figure 3.5) located between the EBIT and the spectrometer entrance. Mirror d in figure 3.5 is only installed due to space constraints. Since the focal length of the lenses is wavelength dependent, the mirror M1 and the lens L4 (a and e in the figure 3.5) need to be adjusted in order to optimize the alignment and the focus on the spectrometer entrance slit (section 3.3.2).

The calibration lamp is connected to this setup via an optical fibre (figure 3.4) and a diffuse aluminium reflector. For the optimal intensity of the calibration lines, the light is focused on the fibres entrance using two lenses.

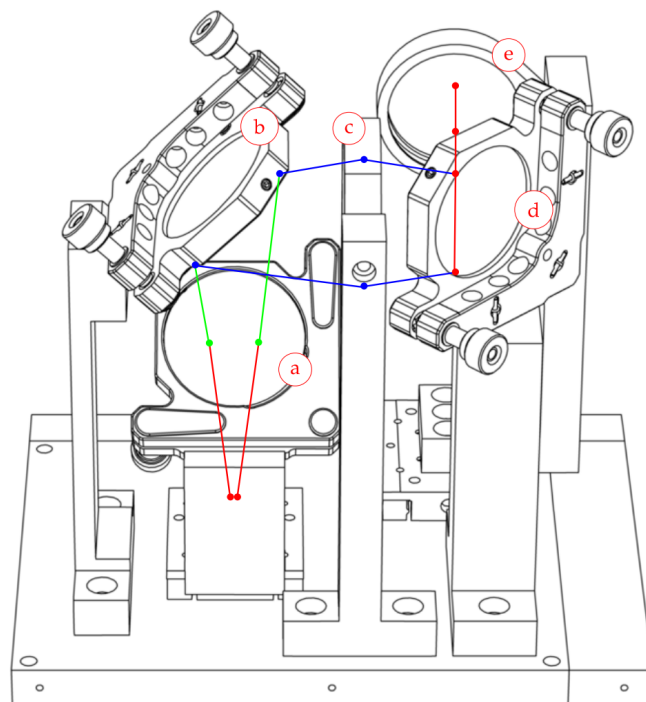


Figure 3.5 Image rotation system as viewed from the EBIT centre. It consists of three mirrors (a,b,d) and two lenses (c,e). Mirror a and lens e are adjustable in direction of the optical axis and determine focus and horizontal alignment of the rotated image. This drawing was done in 2009 [30] for the old spectrometer but the used system is in principle the same.

3.2.2 Spectrometer

In this experiment, a Czerny-Turner monochromator was used. As visualised in figure 3.6, the light A enters the spectrometer through the entrance slit B, is reflected and collimated by the first concave mirror C to the diffraction grating D, which separates the individual wavelengths. Another concave mirror E is used to guide the light through the exit slit F to the CCD camera G. The advantage of this setup is that the profile of the light beam is not broadened [31]. The two identical mirrors C and E compensate each other's astigmatic effects [31]. Since the resolution is also determined by the slit width, the effect of broadening would result in a worse resolved spectrum.

The principle of the diffraction grating is based on constructive interference of the light beams of equal wavelengths at a certain angle. Constructive interference occurs when those light beams, after the reflection from the grating, are aligned and shifted by a path difference equal

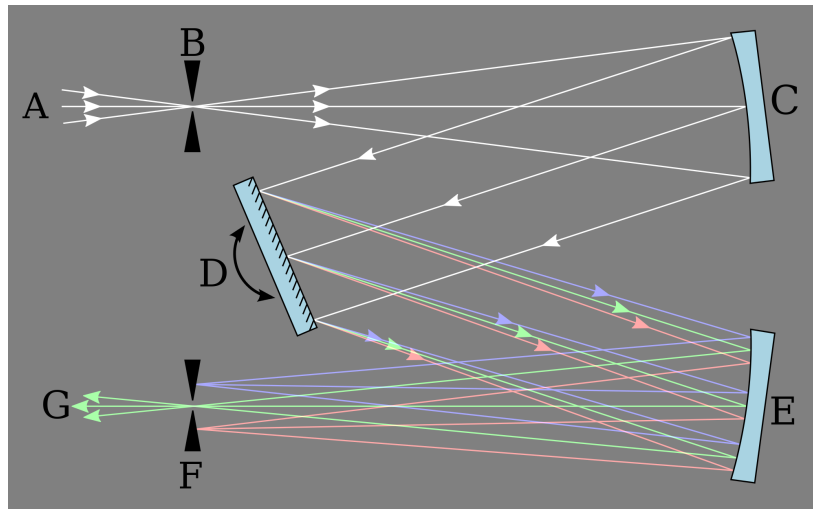


Figure 3.6 Schematics of the Czerny-Turner monochromator with two slits (B,F) two concave mirrors (C, E) and a diffraction grating (D). Different wavelength are visualised by the coloured lines. [32]

to an integer multiple of the wavelength. From this the geometrical interference condition is derived:

$$d \cdot (\sin \theta_i + \sin \theta_m) = k \cdot \lambda \quad (3.2)$$

where θ_i and θ_m are the incident and reflection angles (figure 3.7), d is the distance between two steps of the grating and the integer k is the diffraction order.

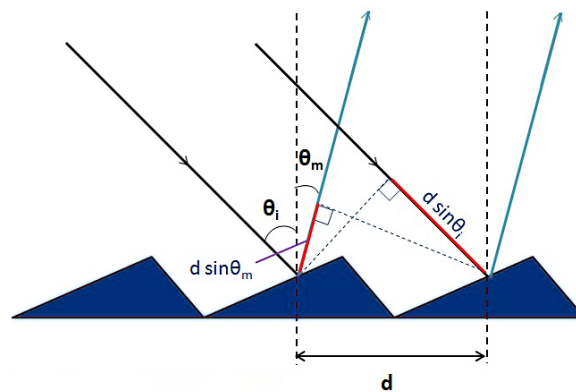


Figure 3.7 Interference at the diffraction grating. The incident light beams (black) are reflected (cyan) off the grating (blue). The path difference of the two beams is visualised in red. ([33] modified)

Dispersion is the property of the grating which relates the change of reflection angle to the corresponding change in wavelength. For a fixed incident angle equation 3.2 leads to:

$$\frac{\partial \theta_m}{\partial \lambda} = \frac{k}{d \cos \theta_m}. \quad (3.3)$$

This equation states important properties of the spectrometer. The dispersion is directly proportional to the diffraction order and the inverse grating line width, which is called line density. For lower wavelengths the dispersion is smaller.

In this work, the monochromator 'Model 2062 Scanning Monochromator' by Mc Pherson with a focal length of 2 meter was used. Besides the stated principle of the Czerny-Turner monochromator, this model has an additional mirror to guide the light beam to the camera. Instead of the exit slit F in figure 3.6, the CCD resolves the different wavelength due to its localized detection of the photons.

3.2.3 CCD

A charged-coupled-device (CCD) camera is used to detect and accumulate the light from the monochromator. A CCD was chosen as it has a large quantum efficiency and a relatively low noise level. The CCD chip is a two-dimensional array of small photon sensitive sensors, the pixels. The sensor is a doped semiconductor (e.g. p-Si) underneath a transparent and electrical-insulating layer (e.g. SiO₂) (see figure 3.8). On top of that is a transparent, electrical-conducting layer, which are the pixels electrodes. When a voltage between the electrode and the semiconductor substrate is applied, a potential well forms at the interference between the substrate and the insulating layer. Electrons excite into the conduction band of the semiconductor by incident photons and create electron-hole pairs. These charges are collected in the potential well.

After the acquisition, the charges in the potential wells are moved to the neighbouring pixels. This is done until all pixel are read out at the end of each column. The charges are converted in a digital signal by the analog-to-digital converter (ADC), which is based on the proportionality of photons and their induced charges. Because the ADC cannot work with negative currents, an offset is added by the ADC (determined in section 4.1). The read out procedure adds a noise to the signal, which can be reduces by 'binning'. Therefore, multiple vertical pixels are combined before the read out procedure. The combined pixel

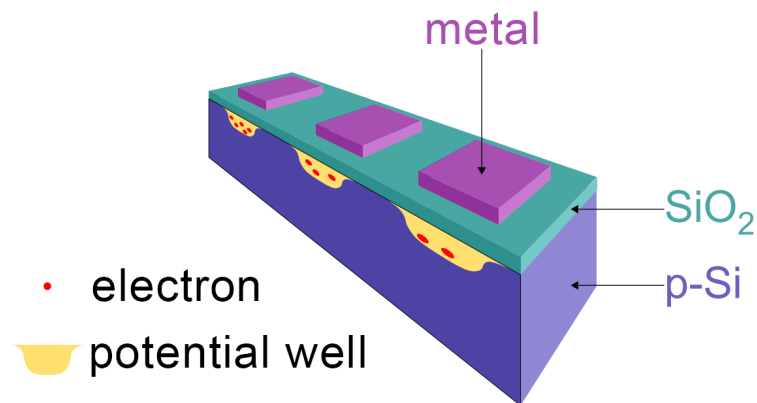


Figure 3.8 Schematics of the CCD chip ([24] modified)

have approximately the same absolute read out noise as one sub pixel before and thus reducing the total noise significantly. The spectral resolution is not effected by binning because it is determined by the horizontal pixels (dispersion axis).

Noise occurs due to thermal excitation in the semiconductor. The CCD chip is therefore cooled, in this case with a Peltier element.

For this measurement, the Andor Newton DU940P CCD camera was used. Its CCD chip has $2048 \cdot 512$ pixel of size $(13.5 \mu\text{m})^2$ and is cooled to -80°C . The read out noise for a full vertical bin of this individual camera is 3.4 counts [34].

3.2.4 Polariser

A wire grid polariser is used to quantify the effect of polarisations on the spectrometer's efficiency. It consists of an array of parallel metallic wires and based on the principle of electromagnetic induction. The electric field component E of the electromagnetic wave induces a movement of electrons in the wire. The energy transfer is very much dependent on the orientation of the wave relative to the wires (figure 3.9). In case E is perpendicular to the wire, the movements of the electrons in the wire are constraint, due to a small expansion in this direction. The energy transfer is small, and the wave passes through the grid. When E is parallel to the wires, the movement of the electrons is relatively large. The energy transfer is large, and the wave is reflected similar as an electromagnetic wave is reflected from a metal

surface. Thus, the light is transferred for polarisations perpendicular to the wires (figure 3.9). This design has the advantage of relatively small dependency of the extinction ratio (figure 3.10) on wavelength and angle of incident. The extinction ratio is a value which gives the ability to reduce the intensity of light perpendicular to the transmission axis.

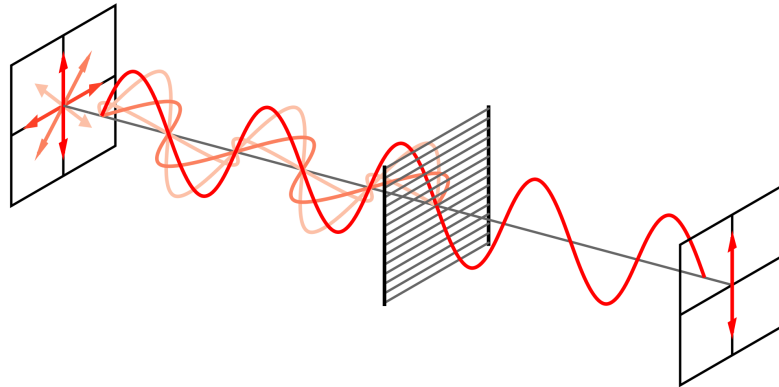


Figure 3.9 The wire grid polariser reflects polarised light, except the polarisation perpendicular to the wires. The electromagnetic wave travels from the left to the right side of the graphic. [35]

In this experiment, a Thorlabs WP25M-UB is used, where the array of metallic wires is between two layers of fused silica. This polariser has a broad band of transmission wavelengths ranging from (250-4000) nm.

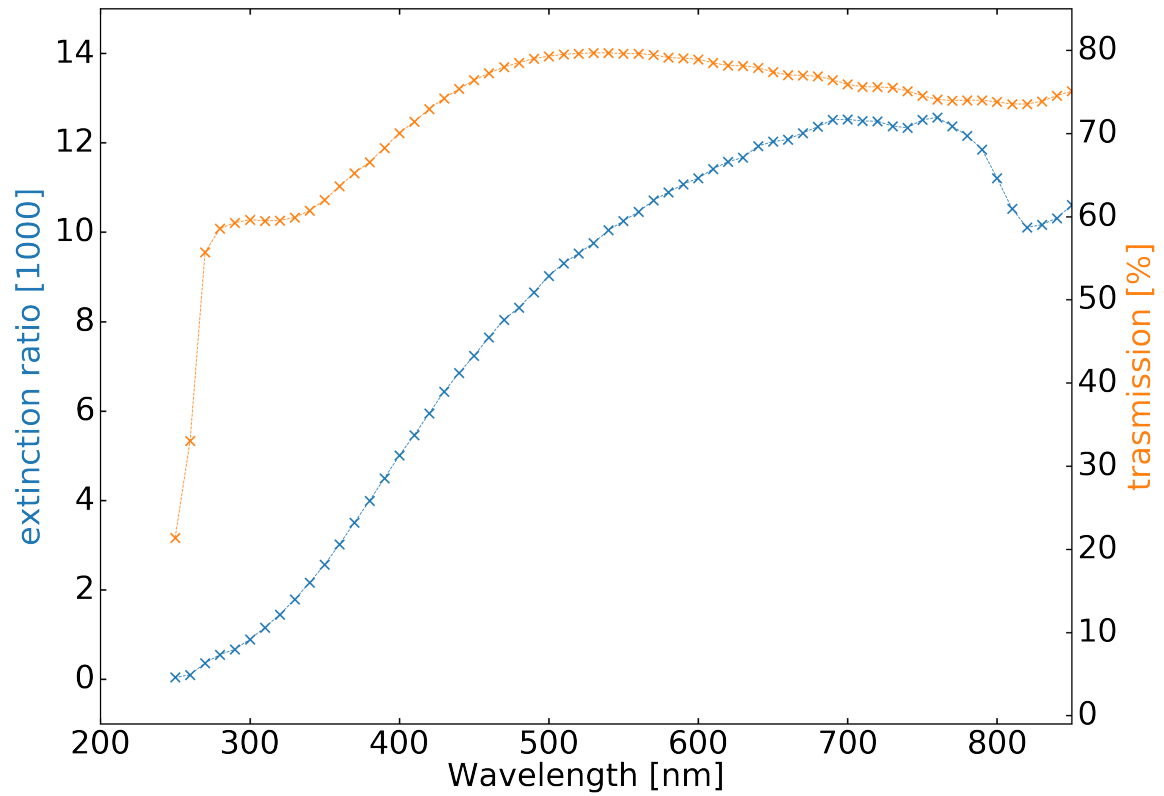


Figure 3.10 Extinction ratio of two perpendicular polarisations (blue) and the transmission of the polarisation which is align (orange). The plot shows the wavelength range later used in the measurement. (Data form [36])

3.3 Measurement

In order to measure the spectra of the HCI, the EBIT and the optical setup need to be adjusted for each individual line.

3.3.1 Adjusting the EBIT

Fe is injected from the bottom side of the central drift-tube in the form of $\text{Fe}(\text{CO})_5$. This liquid vaporizes at room temperature and enters the EBIT trough a needle valve which is used to adjust the injection pressure p_{inj} . The electron beam energy in the trap centre is less than the potential difference of cathode and central drift tube U_{EBIT} , due to the space charge. Hence, higher energies than the ionisation itself requires are needed (see table 3.1). The electron beam energy U_{EBIT} is optimized for maximum intensity of the spectral line. U_{EBIT} needs to be high enough to be able to ionise the required charge state, but not much higher not to ionise other charge states. In table 3.1 the U-U-U notion corresponds to the potentials of the three central drift tubes. Important to notice is the much larger diameter of the central drift tube (5 mm compared to 1.5 mm [25]). A voltage offset of U_{allDT} is applied additionally to all nine drift tubes. The trap is optimized for the lowest possible potential which traps most of the ions in the selected charge state. A low trap is required because evaporative cooling is enhanced for shallow traps. To empty the trap of unwanted ions, dumping is performed every 3 minutes, applying 100 V at the central drift tube.

Table 3.1 Parameter of the EBIT setup

line	ionization energy (eV) [37]	I_{beam} (mA)	U_{cath} (V)	U_{EBIT} (V)	U_{allIDT} (V)	trap configuration (V)	P_{inj} (10^{-9} mbar)
Fe ⁹⁺ at 637 nm	262.7	12	-250	275	5	10-20-10	14
Fe ¹⁰⁺ at 789 nm	292.8	15	-280	300	10	10-10-10	19
Fe ¹²⁺ at 339 nm; 435 V	357.7	20	-350	435	45	10-40-10	12
Fe ¹²⁺ at 339 nm; 440 V	357.7	20	-350	440	40	10-50-10	
Fe ¹³⁺ at 530 nm	390.2	20	-400	470	30	10-40-10	9

3.3.2 Adjusting the optical setup

The optical path from EBIT to spectrometer needs to be adjusted for each wavelength because the focal length of the lenses are wavelength dependent, due to the wavelength dependency of the refractive indices (table 3.2). The light beam is focused with lens L4 on the entrance slit. Therefore, the lens position is optimized by comparing the intensity of a test line at multiple positions. The alignment of slit and light beam is modified by the mirror M1. It is optimized by comparing the line position for a very large entrance slit with a small one. When the line position is not dependent on the slit width, slit and light beam are align.

Spectral resolution is improved by a high line density of the grating, as equation 3.3 states, but the angel exceeds the measurable range for lager wavelengths.

To calibrate the Fe spectra, hallow-cathode lamps with Fe-Ar and Pt-Ne where used. These lamps have many transitions in the required range, so multiple lines can be observed and used for the calibration. Acquisition time and lamp current are chosen such, that the calibration lines have sufficient intensities.

Table 3.2 Parameter of the optical setup

line	grating (lines/mm)	L 4 (mm)	M 1 (mm)	slit (μm)	calibration lamp	lamp current (mA)	calibration time (min)	number of acquisitions
Fe ¹²⁺ at 339 nm	3600	24.0	6.0	100	Pt-Ne	7	3	14 and 16
Fe ¹³⁺ at 530 nm	1800	13.0	5.87	50	Pt-Ne	7	2	35
Fe ⁹⁺ at 637 nm	1800	12.0	5.71	100	Fe-Ar	12	3	22
Fe ¹⁰⁺ at 789 nm	1800	8.0	5.79	100	Fe-Ar	10	3	45

3.3.3 Measuring procedure

In order to obtain a high precision spectrum, a long acquisition time is required to reduce the relative statistical uncertainty. The acquisition time for the Fe spectra is chosen such that the interval of calibration is sufficiently small. For shorter times, the read out noise would have a larger effect on the spectrum. For longer times, the amount of counts induced by comic particles would grow to large and to many pixels would need to be discarded. The measuring sequence consists of:

- 2-3 minute calibration lamp acquisition
- two 5 second clean images
- 30 minute Fe spectrum

This procedure usually continues for one night, until the adjustments for the next line begins. The 5 second acquisitions are for cleaning the CCD from previously accumulated charges. After the whole sequence one to three background measurements were acquired with the EBIT trapping potential inverted, thus empty of ions as sources of the to be measured radiation.

Chapter 4

Analysis and Results

The goal of the analysis is to extract the most precise possible values for the centre wavelength and for the g -factors of each line. For that, the raw data from the spectrometer needs to be processed to finally compile a single spectrum. This is then fitted with an appropriate model. This chapter follows the chronological order in which the Fe spectral lines were measured and processed. The individual analytical steps are shown first, leading to the results of the lines.

4.1 Processing of the Spectra

The processing consists of

- removing pixels influenced by cosmic particles
- background subtraction
- subtraction of the ADC offset induced by the camera
- calibration of the individual spectra (section [4.2](#))
- composition of the final spectrum

The Fe spectra have an acquisition time of 30 minutes. In this long period, it is likely for the CCD camera to detect cosmic charged particles which introduce a large charge in a pixel. Because they usually affect single pixels, they can be removed relatively easily by comparing each pixel with its surroundings, i.e. using the Wojtek Pych [38] algorithm implemented by Bekker [28] and Blessenohl [24].

For background correction, between one and three 30 min background spectra are averaged and smoothed along the dispersive axis to minimize statistical noise. This was done using a moving average filter of window size 30 pixels.

The CCD analog-to-digital converter (ADC) cannot work with negative values, and hence adds a voltage offset. This value was measured in multiple very dark images with minimal acquisition times, so that thermal noise and counts, due to stray light, was negligible. The average of all those images and pixel result in $offset_{ADC} = (300.46 \pm 0.74)$ counts.

After these effects are taken into account, each spectrum is individually calibrated (section 4.2). These calibrated spectra are then summed to obtain the final spectrum. The counts are summed to consider all photons observed from the Fe line and calculate a statistical uncertainty using Poisson statistics. After the individual calibration of the Fe spectra, the same pixel in each spectrum assigns to a different wavelength. Thus, the spectra cannot be added by adding the counts for each pixel. Also, using all the wavelength would end up in $2048 \cdot n$ data points (where n is the number of spectra in the sequence). To compensate statistical variations, the wavelengths are rebinned to 2048 bins, thus creating a spectrum of the original dimensions.

4.2 Calibration procedure

The spectrum measured by the camera is the projection of the 2D images along the non-dispersive axis. Therefore, all the counts in a vertical pixel column are summed creating an array of horizontal positions in pixel with the corresponding counts.

Calibration is the process of relating pixel to the corresponding wavelength. As stated in section 3.2.2, this relation is determined by the cosine function of the diffraction grating. This is approximated in second order by the polynomial:

$$\lambda(pix) = a + b \cdot pix + c \cdot pix^2 \quad (4.1)$$

where a, b, c are fit parameters, pix the pixel position and λ the resulting wavelength. To perform this fit, at least five lines in the calibration spectrum need to be identified with lines of the NIST (National Institute of Standards and Technology, USA) database (e.g. figure 4.5).

To reduce the impact of changing environmental conditions on the calibration accuracy, e.g. changing temperature, for every spectrum of the measurement sequence one calibration spectrum was acquired. Changing temperature can affect the setup of the spectrometer due to expansion and contraction of the metal frame.

The calibration spectra do not change much between two acquisitions (table 4.1). This is indicated in figure 4.1, where the shift of one calibration line, in the course of all Fe¹³⁺ acquisitions is plotted. Nevertheless, two of the calibration spectra are used for one Fe spectrum by taking the mean of the calibration before and after the to be calibrated Fe spectrum.

The overall shift for the whole sequence is not neglect able, with about 2.6 nm. Therefore, the calibration interval of 30 min is chosen as the mean shift, using the average of two calibrations, is in the order of the two last significant digits in the measured Fe line (table 4.5).

Table 4.1 Statistics on the differences of the second peak positions of two successive calibration spectra for the Fe¹³⁺ at 530 nm line.

	pixel	wavelength (nm)
maximum	0.558(3)	0.00178(4)
mean	0.069	0.00022
standard deviation	0.177	0.00056

In order to assign NIST reference lines to the lines in the calibration spectrum (e.g. table 4.3), one of the spectra needs to be calibrated by hand. The range of wavelength observed in the spectrum is approximately 6 nm for the 1800 lines/mm grating and 3 nm for 3600 lines/mm grating. Due to the difficulty of identifying enough lines, another spectrum was acquired using a 150/mm grating with a wavelength range of approximately 90 nm. Using this larger range spectrum, the most intense lines of the included small spectral range could be calibrated, what led to an orientation for the identification of more lines in the smaller range.

Based on this identification of the lines, the assignment for the other calibration spectra was performed automatically. This was done using the python program AutoCal.py [28].

For the uncertainty of a single calibration λ_{single} , the half width of the 68.3% confidence band at the respective Fe line wavelength was used, as seen in figure 4.2. With error propagation,

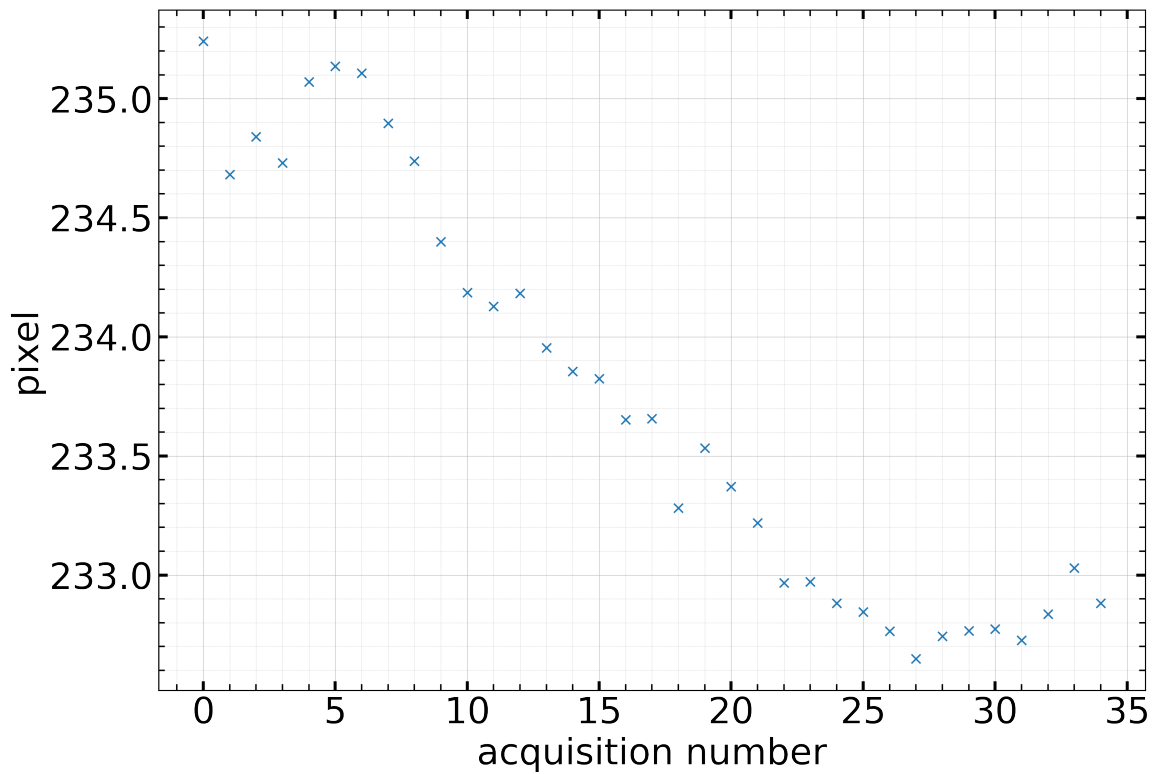


Figure 4.1 The peak position of the maximal peak in the Fe^{13+} at 530 nm calibration spectra against the number of the acquisition. The position fit uncertainties are not perceptible in this plot.

the total calibration uncertainty was calculated:

$$\Delta\lambda_{\text{total}} = \frac{\Delta\lambda_{\text{single}}}{\sqrt{n}}. \quad (4.2)$$

This uncertainty approximation is based on the assumption that the uncertainty for each individual calibration spectrum is equal. This was confirmed for multiple randomly chosen calibration spectra of each Fe sequence. Also, the AutoCal.py results indicate when an automatic calibration was not successfully, thus a considerably less accurate calibration of a single spectrum can be avoided.

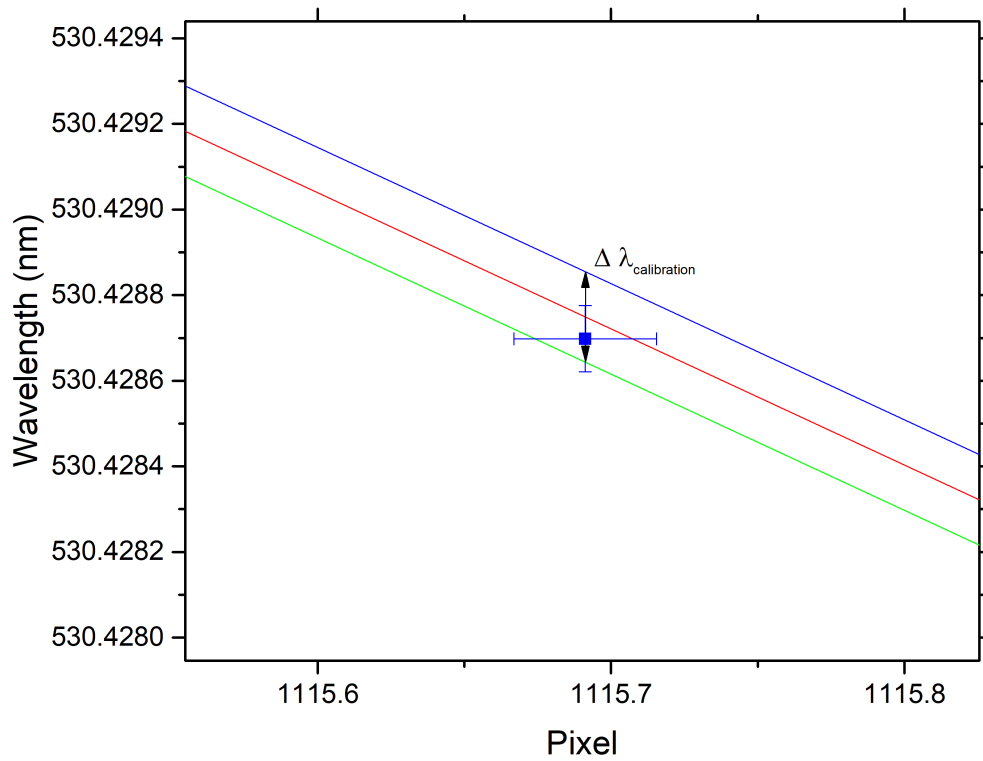


Figure 4.2 Calibration polynomial (red), of the Fe^{13+} line, with 68.3% confidence band and the Fe line measurement to approximate the uncertainty of the calibration.

4.3 Zeeman fitting model

The Zeeman splitting of the Fe lines is predictable by theory. The following model is based on section 2.3. To work with energies rather than with wavelength, the wavelength are converted using:

$$E = \frac{hc}{\lambda_{vacuum}} \quad (4.3)$$

Here, the values for h and c , as recommended by CODATA, were used [39]. The conversion from air to vacuum wavelength was done according to [40], which models the refraction of air in normal conditions:

$$\lambda_{vacuum} = n_{air} \cdot \lambda_{air} \quad (4.4)$$

$$= \left[1 + 10^{-8} \left(8342.13 + \frac{2406030}{130 - \left(\frac{1000}{\lambda_{air}}\right)^2} + \frac{15997}{38.9 - \left(\frac{1000}{\lambda_{air}}\right)^2} \right) \right] \cdot \lambda_{air} \quad (4.5)$$

The Zeeman fitting model uses convolutions of Gaussian functions for each substructure line.

$$\begin{aligned} & f(E_0, w_{Gaussian}, A_0, A_{\pm 1}, offset) \\ &= offset + \sum_{\text{all transitions}} A_{\Delta M} \langle j_f(m_i + \Delta m) \mathbb{1}_{\Delta m} | j_i m_i \rangle^2 \cdot Gaussian(E_0 + \Delta E_z, w_{Gaussian}) \end{aligned} \quad (4.6)$$

where $j_{i,f}$ are the j values of the initial and final states. This model is based on the following assumptions:

- separation of all substructure lines are given by $\Delta E_z(g_j^i, g_j^f)$ to the centre energy E_0
- relative intensities of the lines are given by the Clebsch-Gordan coefficients which lead to the $\langle j_f(m_i + \Delta m) \mathbb{1}_{\Delta m} | j_i m_i \rangle^2$ term
- the effect of the optical setup on the intensity relation of the orthogonally polarised lines is parametrized by A_0 and A_{\pm}
- the Zeeman model is formed by convolution of the individual lines with Gaussian profiles of width $w_{Gaussian}$

The g -factors for $\Delta E_z(g_j^i, g_j^f)$ are either free fit parameters or calculated using the Landé g -factor equation 2.21. Thus, for well-separated substructure lines, g -factors can be determined from the measured data. Note that both g -factors are correlated as g_f determines the energy

separation from the centre to the Δm sets and $g_i - g_f$ determines the separation within those sets. The model and software implementation is based on works of Hendrik Bekker [28].

4.4 Uncertainty of the counts

The statistical uncertainty on the photon counts was calculated using Poisson statistics. For this uncertainty, the background counts need to be considered as well, since they also affect the data. Hence, the statistical error on the counts of each data point is:

$$\Delta C_{\text{stat}} = \sqrt{C_{\text{processed}} + C_{\text{background}} - \text{ADC offset}}.$$

Where $C_{\text{processed}}$ is the number of counts after the whole previously stated procedure, including the background and ADC offset subtraction.

As mentioned in section 3.2.3, the camera read out procedure of the pixels leads to a considerable uncertainty on the counts. Using error propagation, the read out uncertainty is

$$\Delta C_{\text{read out}} = \sqrt{n \cdot b} \cdot \Delta C_{\text{full vertical line}} \quad (4.7)$$

where b is the number of vertical bins in the spectrum and $\Delta C_{\text{full vertical line}}$ is the read out noise on one vertical pixel column, given by the camera manufacturer [34]. The read out uncertainty for the Fe^{13+} line is approximately 110 counts.

Thus, the total uncertainty on the counts is

$$\Delta C_{\text{total}} = \sqrt{(\Delta C_{\text{stat}})^2 + (\Delta C_{\text{read out}})^2} \quad (4.8)$$

4.5 Measured spectral lines of Fe ions

4.5.1 Fe¹³⁺ at 530 nm

The first of the measured iron lines in this work is the ${}^2P_{1/2} \rightarrow {}^2P_{3/2}$ M1 transition of Fe¹³⁺. The Zeeman theory predicts six components, as seen in figure 4.3. All of those sub-structural lines can be resolved without overlap, so the level of counts in between the lines is on the background level. The individual lines have, as expected, Gaussian profiles. For the Zeeman model, a fit with the g -factors as fit parameters and with g -factors from Landé was performed. In figure 4.4a, a small shift of the peaks is perceptible. This shift increases with the distance from the centre and is also apparent in the residual plot 4.4b where the residuals for the Landé model increase from the centre. The residuals are more homogeneously distributed for the free g -factors fit and therefore indicate the use of an appropriate fitting model. In table 4.2 the fit parameters, according to both models, are listed. The difference in line centres is 2.3σ and is therefore significant. Line width and g -factors also deviate significantly (line width: 3.0σ , g_i : 105σ , g_f : 27.9σ). Both χ^2 values indicate a relatively good fit, but also small underestimation of uncertainties of the data points as this value is supposed to be one. Based on this, the results of the g -factors as fit parameters are used for further analysis.

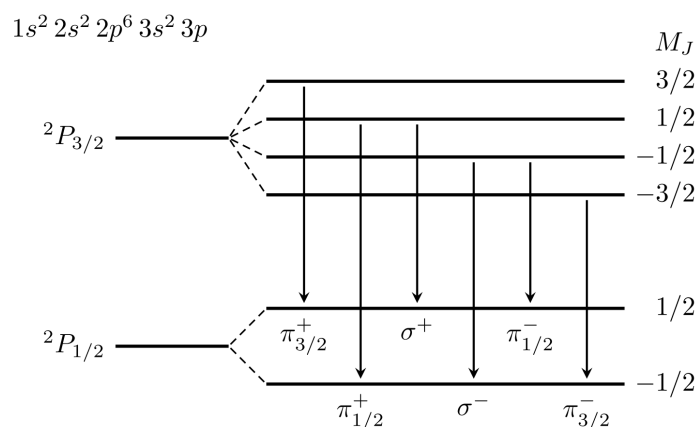
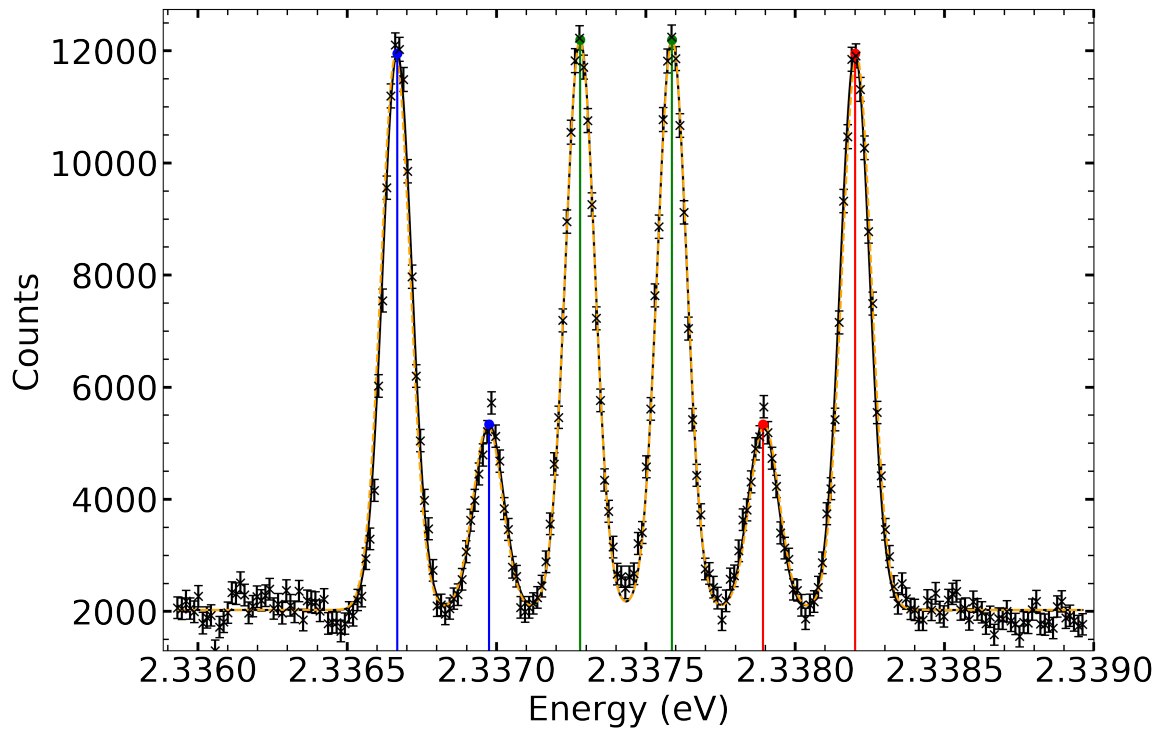
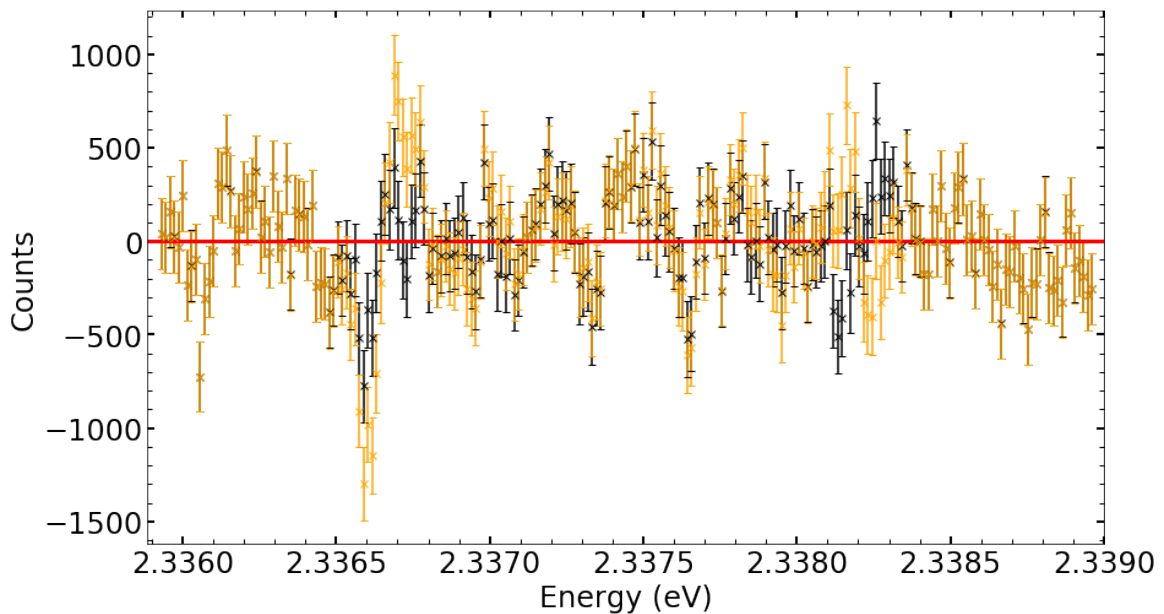


Figure 4.3 Components of the Zeeman splitting originate from the energy substructure. The lines are labelled with $\pi_{3/2}^+$ for the π polarised line from the initial state with $m_j = +3/2$. [23]



(a)



(b)

Figure 4.4 (a) Measurements of Fe^{13+} as black x with error bars. For the black line, a Zeeman fit model was used with g -factors as fit parameters in comparison with the Zeeman model using Landé for fixed g -factors (orange, dashed). The coloured lines blue, green, red indicate the positions of the individual Zeeman components (using the free g -factors) with $\Delta m = -1$, $\Delta m = 0$, $\Delta m = +1$. (b) Residuals of the Zeeman fit with fixed g -factors (orange) and g -factors as fit parameters (black).

Table 4.2 Results of the Zeeman model fit in figure 4.4a

Property	g-factors fix	g-factors free
Line centre (nm)	530.42868(1)	530.42870(1)
Line centre (eV)	2.33743388(4)	2.33743381(4)
Line width (eV)	$4.932(5) \cdot 10^{-5}$	$4.920(4) \cdot 10^{-5}$
g_j initial	4/3	1.3228(1)
g_j final	2/3	0.6583(3)
offset (counts)	2026(27)	2026(22)
χ_{red}^2	2.44	1.53

For the calibration, a Pt-Ne lamp was used. For the identified lines of table 4.3 a second-order polynomial fit was performed in figure 4.5. In table 4.4, the uncertainty on c is nearly as large as the value of c , it means that higher order polynomial would probably not be a better model.

Table 4.3 Lines used for the calibration from NIST [41]

peak (pixel)	wavelength (nm, vacuum)	Ion	NIST reference
155.28	533.47918	Ne I	L4498 [42]
235.2344	533.22603	Ne I	L3451 [43]
373.2803	532.7878	Ne I	L7292
675.63	531.82837	Ne I	L4498 [42]
739.03	531.62637	Ne I	L4498 [42]
1054.536	530.62339	Ne I	L3451 [43]
1172.22	530.249	Pt I	L3475
1260.909	529.96633	Ne I	L3451 [43]
1828.88	528.15546	Ne I	L3451 [43]
2018.03	527.55070	Ne I	L3451 [43]

Table 4.4 Calibration polynomial parameters

a (nm)	b (10^{-3} nm/pix)	c (10^{-9} nm/pix ²)	residual variance
533.971650(8)	-3.168(4)	-6.67(3)	0.96

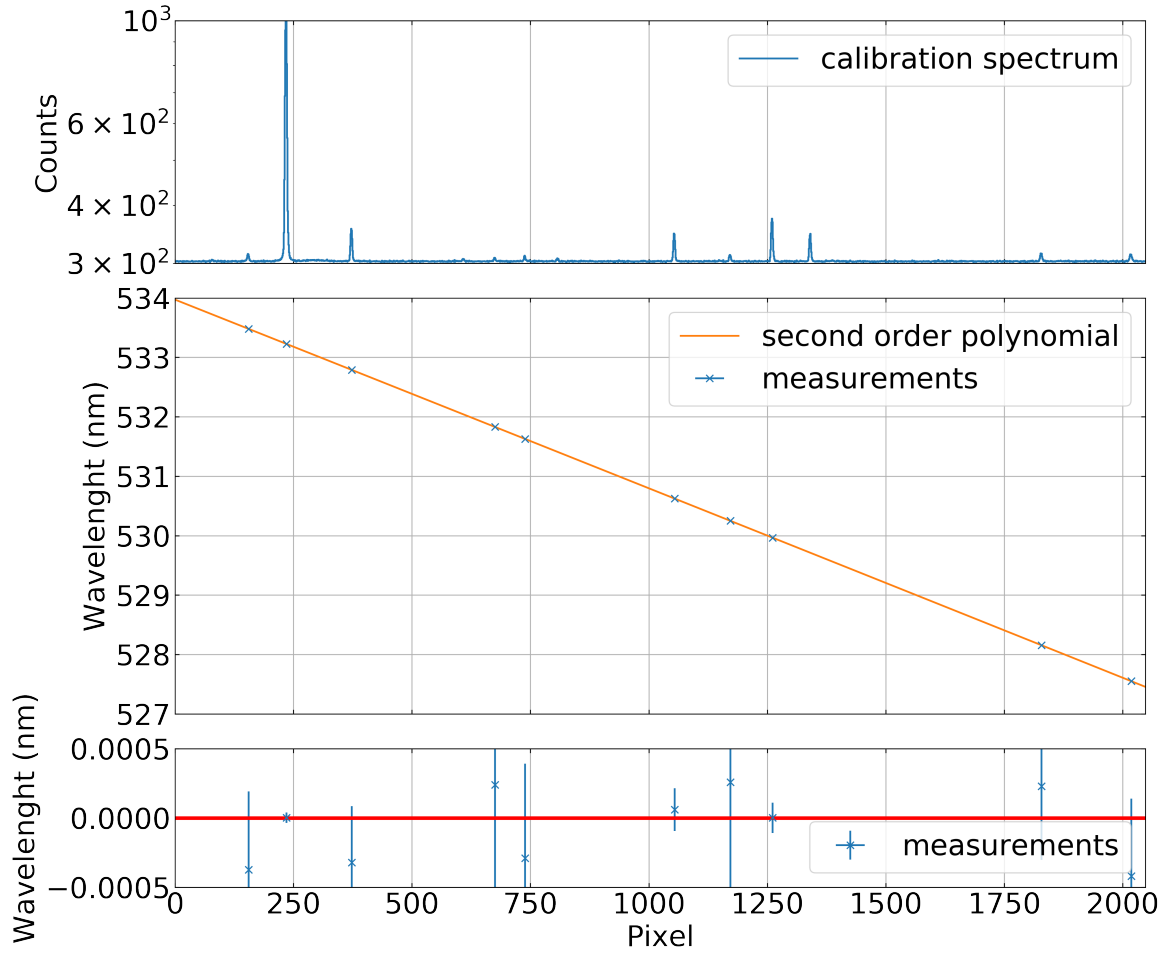


Figure 4.5 Calibration Spectrum of the Pt-Ne lamp, fitted polynomial on the identified peaks, residuals of the fitted data points

The resulting uncertainties for the calibration and the Zeeman fit with g -factors as fit parameters are:

$$\Delta\lambda_{\text{calibration}} = 1.8 \cdot 10^{-5} \text{ nm}$$

$$\Delta\lambda_{\text{Zeeman fit}} = 7.7 \cdot 10^{-5} \text{ nm}$$

$$\Delta\lambda_{\text{total}} = 7.9 \cdot 10^{-5} \text{ nm}$$

The deviation of the centre wavelength from the reference works (table 4.5) on this line are all significant, with (+14, +73, +71, +59, -66) σ . It is important to notice that the references deviate significantly among themselves. The reference EBIT measurements, all performed all at the same trap, deviate significantly from Schnorr's measurement with +12 σ . The

solar eclipse observation is not recent and additional effects, e.g. the Doppler shift, were not considered (see section 4.9).

Table 4.5 Results compared to other works on this line. Using the values of the free g -factors. Equation 4.4 was used if the wavelength were given in air.

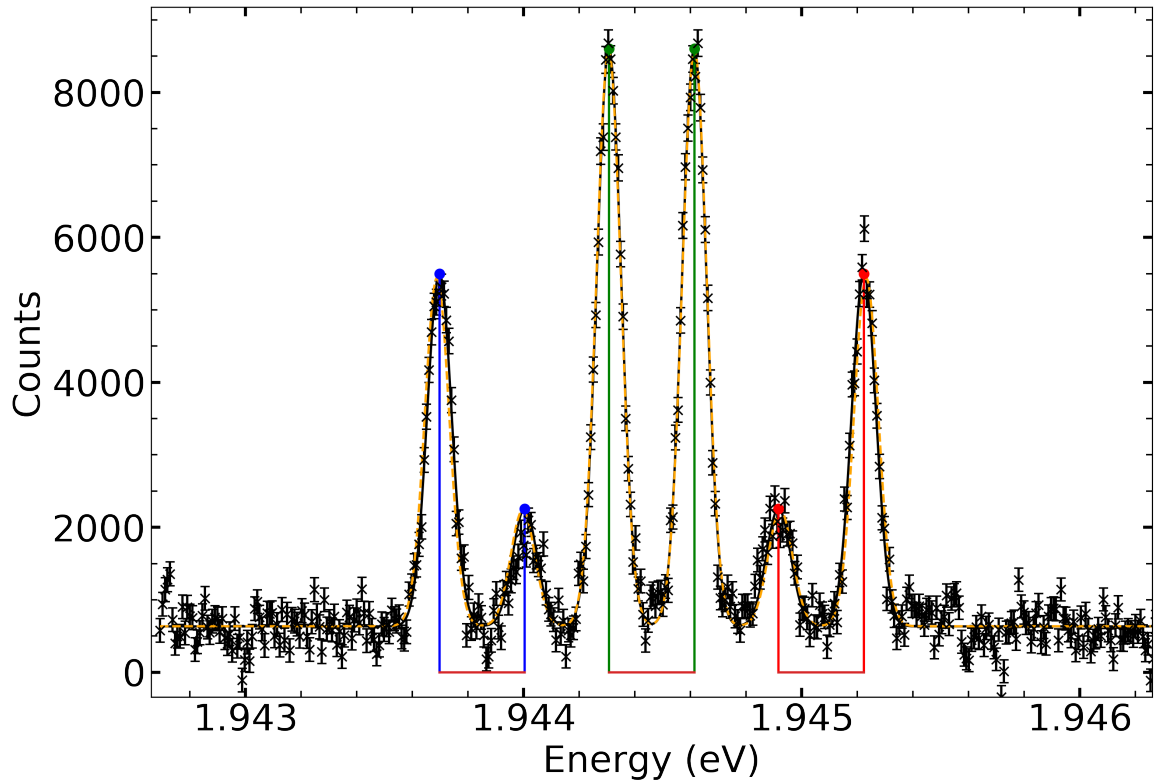
reference	wavelength (nm, vacuum)	
this work	530.42870(8)	
Schnorr 2013, 2011 [7, 23]	530.4276(4)	EBIT laser spectroscopy
Link 2010 [27]	530.4228(1)	EBIT spectroscopy
Arnesh 2014 [44]	530.423(8)	EBIT spectroscopy
Rybanský 1986 [45]	530.4240(5)	solar eclipse observation
NIST: Edlen 1942 [46]	530.434	solar eclipse observation

4.5.2 Fe⁹⁺ at 637 nm

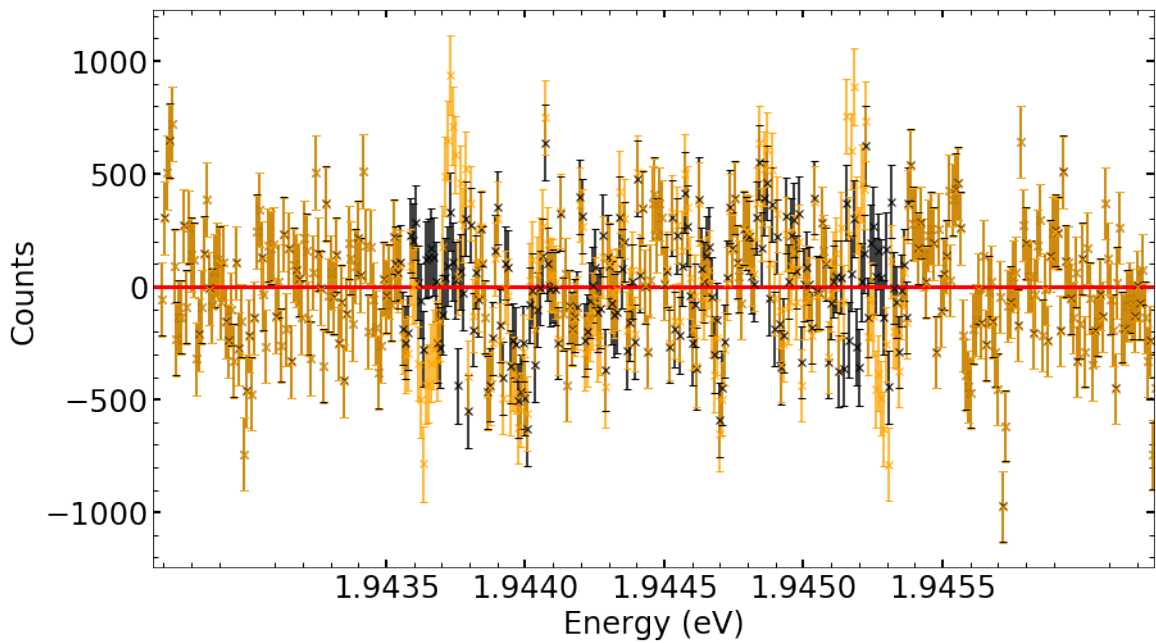
The following line corresponds to the $^2P_{3/2} \rightarrow ^2P_{1/2}$ M1 transition. The results are plotted in 4.6a. The centre positions of the two Zeeman fit models deviate with 14σ from each other. Also, the g -factors deviations are significant. In figure 4.6b the residuals for the fixed g -factors model are not randomly distributed, as the deviation at the regions of the outer components is similar for sets of neighbouring data points. The χ^2 values again indicate the g -variable fitting model to be more suitable.

Table 4.6 Results of the Zeeman model fit in figure 4.6a

Property	g -factors fix	g -factors free
Line centre (nm)	637.6277(2)	637.6277(1)
Line centre (eV)	1.94446055(5)	1.94446069(4)
Line width (eV)	$4.401(5) \cdot 10^{-5}$	$4.382(5) \cdot 10^{-5}$
g_j initial	2/3	0.6541(3)
g_j final	4/3	1.3167(2)
offset (counts)	635(17)	633(15)
χ_{red}^2	3.29	2.55



(a)



(b)

Figure 4.6 (a) Measurements of Fe^{9+} as black x with error bars. For the black line, a Zeeman fit model was used with g -factors as fit parameters in comparison with the Zeeman model using Landé for fixed g -factors (orange, dashed). The coloured lines blue, green, red indicate the positions of the individual Zeeman components (using the free g -factors) with $\Delta m = -1$, $\Delta m = 0$, $\Delta m = +1$. (b) Residuals of the Zeeman fit with fixed g -factors (orange) and g -factors as fit parameters (black).

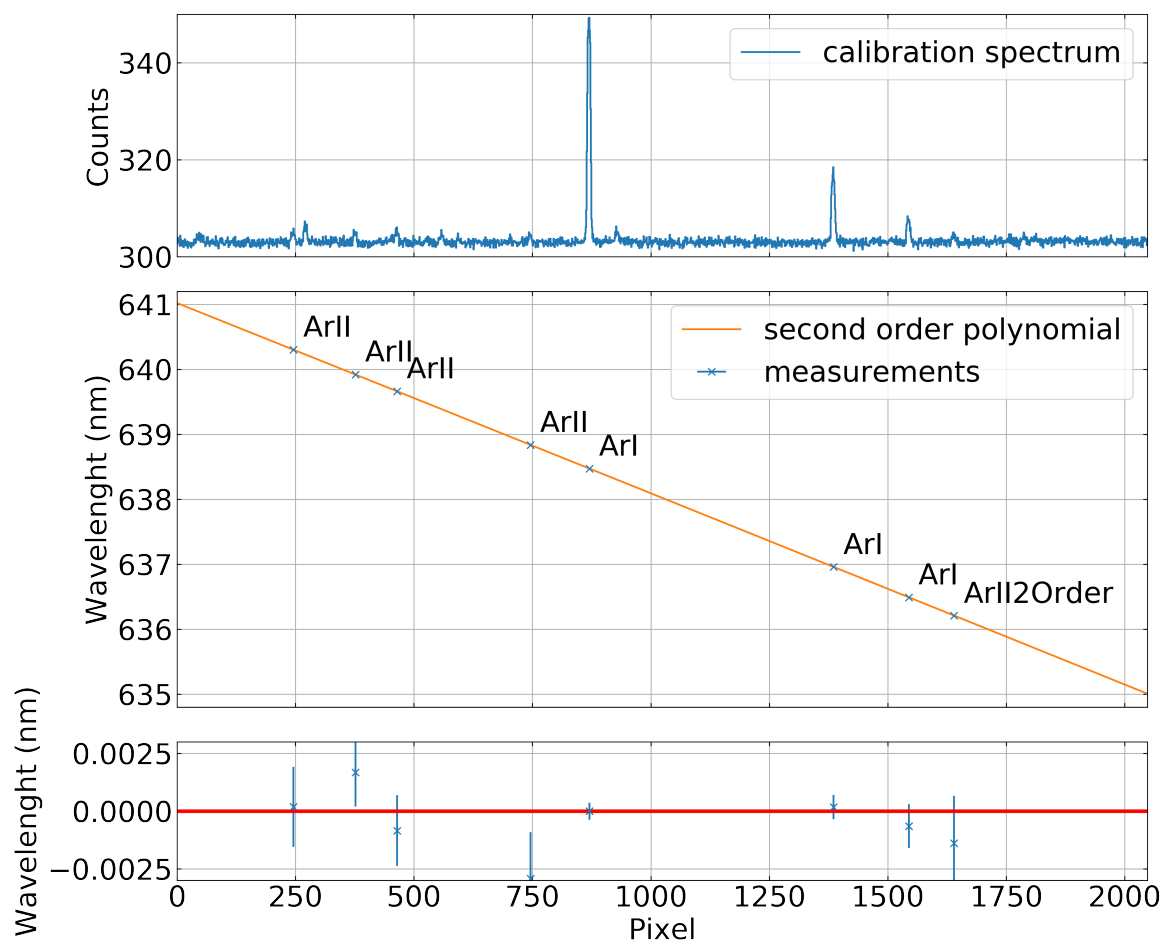


Figure 4.7 Calibration Spectrum of the Fe-Ar lamp, fitted polynomial on the identified peaks, residuals of the fitted data points

Table 4.7 Calibration polynomial parameters

a (nm)	b (10^{-3} nm/pix)	c (10^{-9} nm/pix ²)	residual variance
641.0198(2)	-2.9207(4)	-8(2)	1.29

Table 4.8 Lines used for the calibration from NIST [41]. The Ar II line in second order needs to be divided by two to find the original reference value.

peak (pixel)	wavelength (nm, air)	Ion	NIST reference
245.9	640.30123	Ar II	L11520 [47]
376.5	639.92085	Ar II	L11520 [47]
464.4	639.66084	Ar II	L11520 [47]
745.9	638.8341	Ar II	L11520 [47]
1385.8	636.9575	Ar I	L2634 [48]
870.4	638.4717	Ar I	L2634 [48]
1544.5	636.4894	Ar I	T1218n
1640.0	636.20748	Ar II second order	L11520 [47]

The calibration uncertainty is here much larger than the Zeeman fitting uncertainty and therefore dominates the total uncertainty.

$$\Delta\lambda_{\text{calibration}} = 4.2 \cdot 10^{-4} \text{ nm}$$

$$\Delta\lambda_{\text{Zeeman fit}} = 1.4 \cdot 10^{-4} \text{ nm}$$

$$\Delta\lambda_{\text{total}} = 4.4 \cdot 10^{-4} \text{ nm}$$

The measurement by Brenner on the same EBIT in 2009 differs by -23σ . The measured line differs from the Jefferies measurement with -123σ , but this might be explainable with Doppler shifts occurring in a solar observation (chapter 5). Grotian's line is in good agreement with this measurement.

Table 4.9 Results compared to other works on this line. Using the values of the g -factors as fit parameters analysis. Equation 4.4 was used if the wavelength were given in air.

reference	wavelength (nm, vacuum)	
this work	637.6277(4)	
Brenner 2009 [49]	637.630(1)	EBIT spectroscopy
NIST: Jefferies 1971 [50]	637.64	solar eclipse observation
NIST: Grotian 1939 [5]	637.627	solar eclipse observation

4.5.3 Fe¹²⁺ at 339 nm

This line probably corresponds to the Fe¹²⁺ $^1D_2 \rightarrow ^3P_2$ transition, but the resulting g -factors indicate that this might not be the case. This issue is further discussed in chapter 5.

In this measurement, the trapping potential needed to be changed during the sequence. The two configurations (parameters in table 3.1) are treated as two individual lines before using the mean of these results for the final results. This gives the chance of a little insight in the effect of the trapping potentials on parameters like Doppler broadening and ion cloud temperature (section 4.6).

Table 4.10 435 V EBIT potential: Results of the Zeeman model fit in figure 4.8a

Property	g -factors fix	g -factors free
Line centre (nm)	338.8931(4)	338.8930(2)
Line centre (eV)	3.6585049(4)	3.6585065(2)
Line width (eV)	$1.593(5) \cdot 10^{-4}$	$1.210(3) \cdot 10^{-4}$
g_j initial	1	1.035(3)
g_j final	1.5	1.450(3)
offset (counts)	6711(63)	6728(45)
χ_{red}^2	20.44	10.16

Table 4.11 440 V EBIT potential: Results of the Zeeman model fit in figure 4.9a

Property	g -factors fix	g -factors free
Line centre (nm)	338.8931(4)	338.8930(2)
Line centre (eV)	3.6585046(4)	3.6585059(2)
Line width (eV)	$1.493(6) \cdot 10^{-4}$	$1.105(3) \cdot 10^{-4}$
g_j initial	1	1.080(2)
g_j final	1.5	1.492(2)
offset (counts)	1585(52)	1594(26)
χ_{red}^2	16.77	5.93

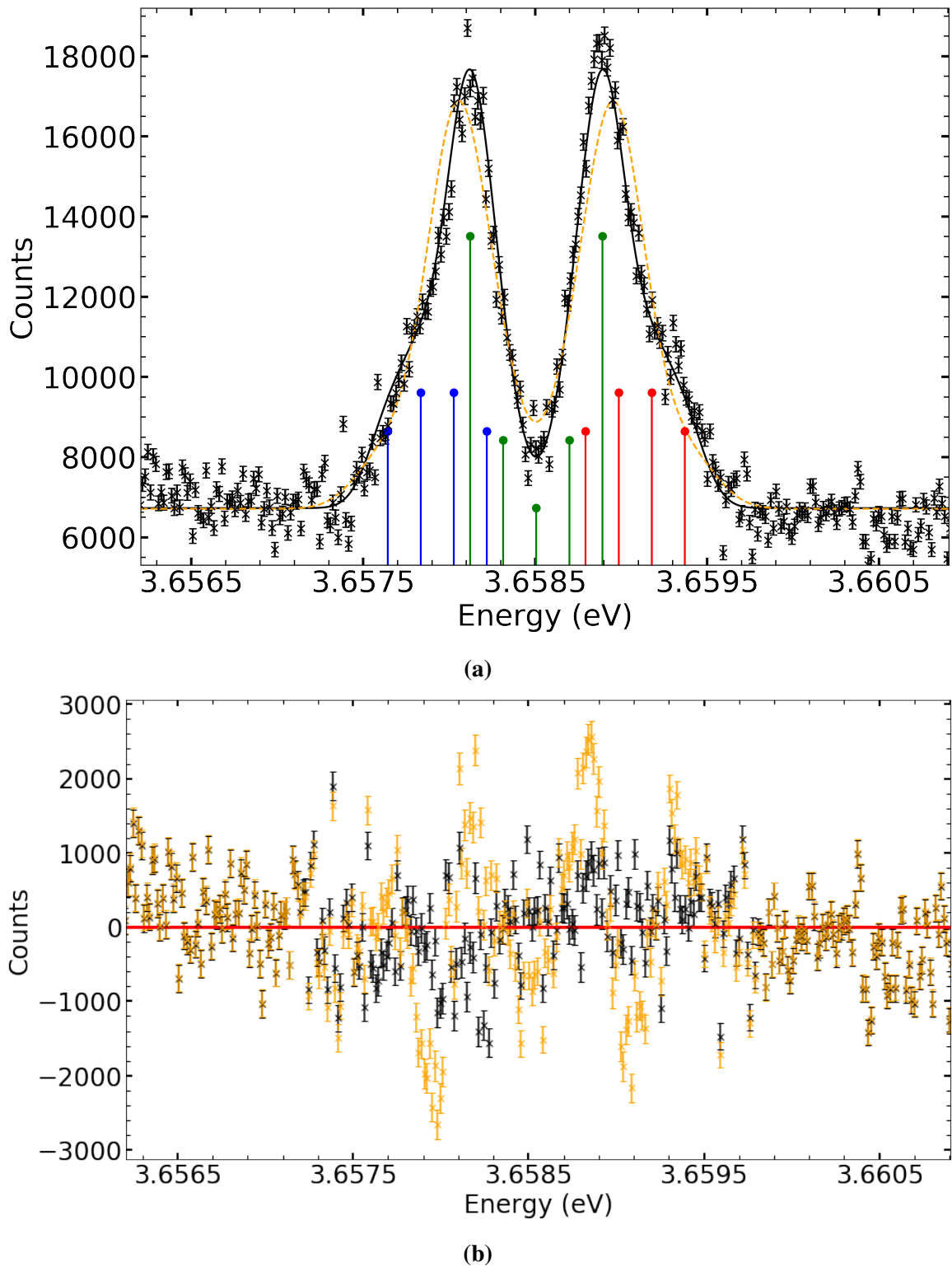


Figure 4.8 (a) Measurements of Fe^{12+} , at 435 V EBIT potential, as black x with error bars. For the black line a Zeeman fit model was used with g -factors as fit parameters in comparison with the Zeeman model using Landé for fixed g -factors (orange, dashed). The coloured lines blue, green, red indicate the positions of the individual Zeeman components (using the free g -factors) with $\Delta m = -1$, $\Delta m = 0$, $\Delta m = +1$. (b) Residuals of the Zeeman fit with fixed g -factors (orange) and g -factors as fit parameters (black).

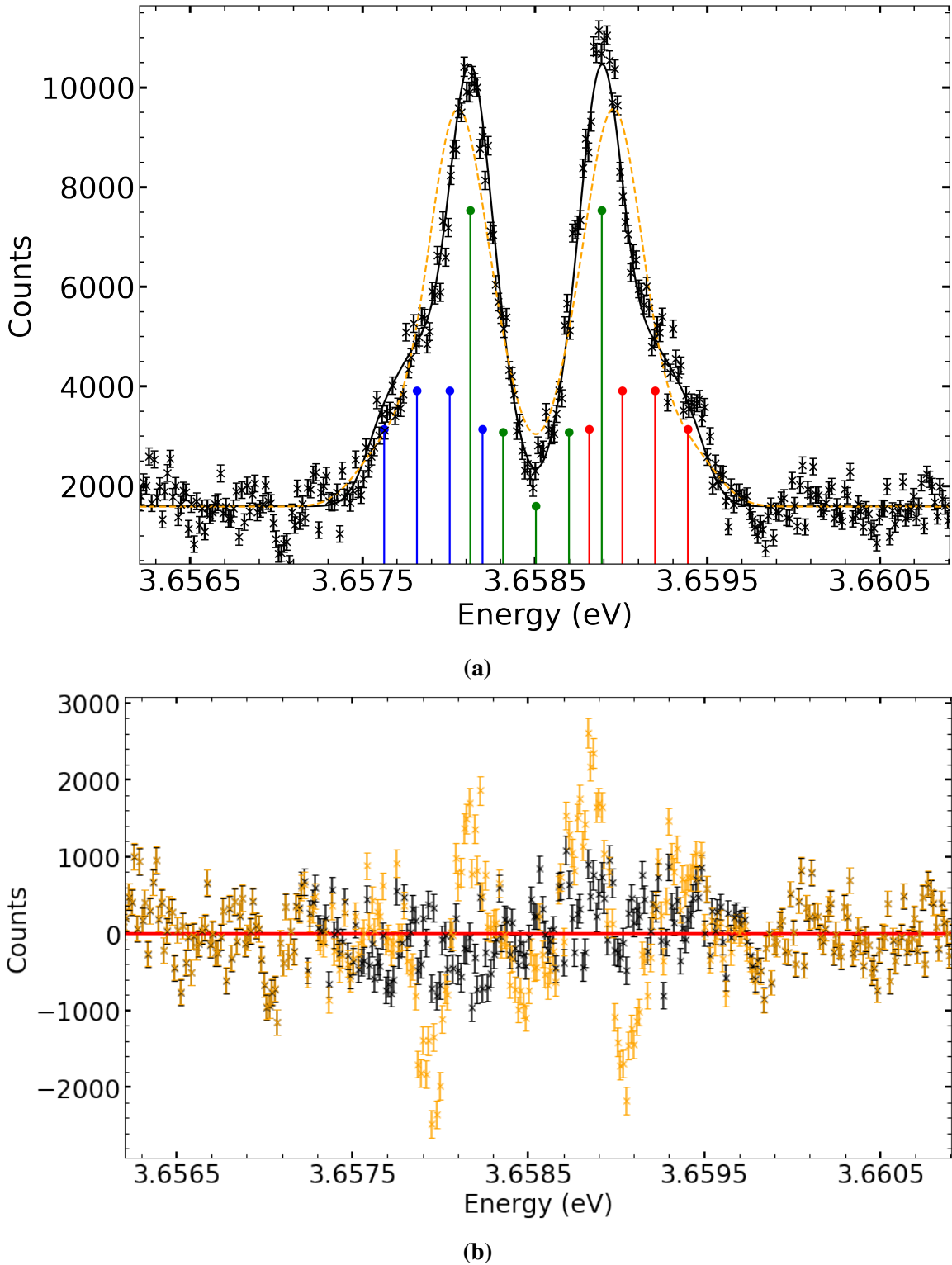


Figure 4.9 (a) Measurements of Fe^{12+} , with 440 V EBIT potential, as black x with error bars. For the black line a Zeeman fit model was used with g -factors as fit parameters in comparison with the Zeeman model using Landé for fixed g -factors (orange, dashed). The coloured lines blue, green, red indicate the positions of the individual Zeeman components (using the free g -factors) with $\Delta m = +1$, $\Delta m = 0$, $\Delta m = -1$. (b) Residuals of the Zeeman fit with fixed g -factors (orange) and g -factors as fit parameters (black).

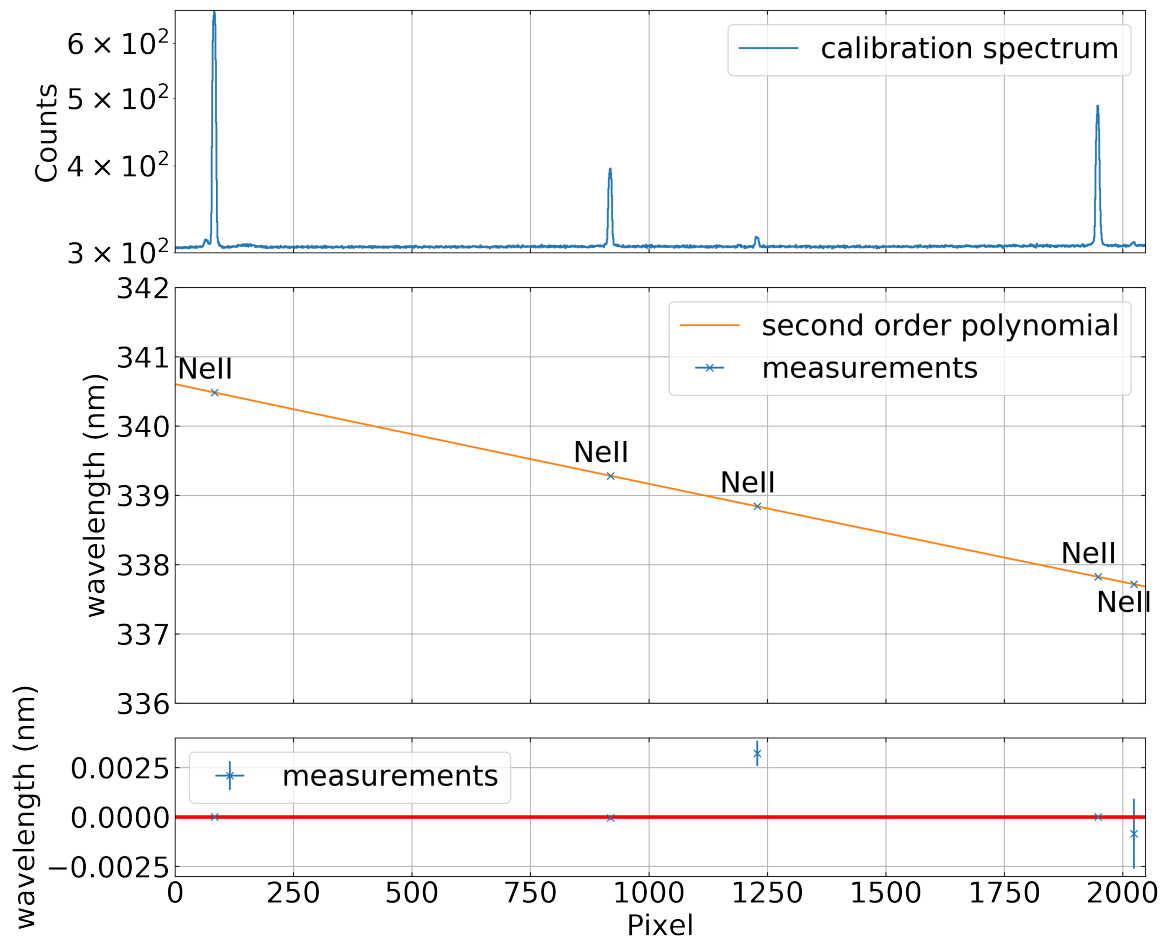


Figure 4.10 Calibration Spectrum of the Pt-Ne lamp, fitted polynomial on the identified peaks, residuals of the fitted data points

Table 4.12 Calibration polynomial parameters

a (nm)	b (10^{-3} nm/pix)	c (10^{-8} nm/pix ²)	residual variance
340.60344(1)	-1.45001(6)	1.145(3)	14.73

Table 4.13 Lines used for the calibration from NIST [41]

peak (pixel)	wavelength (nm, air)	Ion	NIST reference
83.75	340.48208	Ne II	L9088 [51]
919.31	339.28006	Ne II	L9088 [51]
1229.1	338.84169	Ne II	L9088 [51]
1948.23	337.82193	Ne II	L9088 [51]
2023	337.71543	Ne II	L9088 [51]

The calibration uncertainty is again dominating the total uncertainty.

$$\Delta\lambda_{435 \text{ calibration}} = 4.2 \cdot 10^{-4} \text{ nm}$$

$$\Delta\lambda_{435\text{V Zeeman fit}} = 2.2 \cdot 10^{-4} \text{ nm}$$

$$\Delta\lambda_{435\text{V total}} = 4.8 \cdot 10^{-4} \text{ nm}$$

$$\Delta\lambda_{440 \text{ calibration}} = 4.0 \cdot 10^{-4} \text{ nm}$$

$$\Delta\lambda_{440\text{V Zeeman fit}} = 1.9 \cdot 10^{-4} \text{ nm}$$

$$\Delta\lambda_{440\text{V total}} = 4.4 \cdot 10^{-4} \text{ nm}$$

$$\Delta\lambda_{\text{total}} = 3.3 \cdot 10^{-4} \text{ nm}$$

Table 4.14 Results compared to other works on this line. Using the values of free g -factors fit. Equation 4.4 was used if the wavelength were given in air.

reference	wavelength (nm, vacuum)	
this work	338.8930(3)	
Arnesh [44]	338.885(3)	EBIT spectroscopy
NIST: Jefferies 1971 [50]	338.95	solar eclipse observation
NIST: Huang 1985 [52]	338.91	E2 transition, Dirac-Fock calculation

The wavelengths obtained for both trapping potentials are equal for the significant digits. For this transition the Landé g -factor model is not sufficient. The χ^2 values 20.44 and 17.17 indicate a large systematic deviation of model and data. This can also be seen in the residual plots 4.8b and 4.9b, where the residuals are not homogeneously distributed in the regions of the Zeeman lines.

The measured line deviates $+27 \sigma$ from Arnesch, -190σ from the Jefferies lines and -57σ from the Ritz line of Huang.

4.5.4 Fe^{10+} at 789 nm

The ${}^3P_1 \rightarrow {}^3P_2$ M1 transition was measured. For this line, only the baseline subtracted data was used for the fitting, as the fit did not work otherwise. The baseline is a linear function fitted in the closer surroundings of the observed line (figure 4.11). This method is based on the assumption that background subtraction does not sufficiently eliminate the unwanted ambient light. This improves the signal-to-noise ratio which is relatively small for this line. The centre wavelength of the two fitting models is equal for the significant digits. The line width differs largely, by 40σ . The g -factors deviate very differently with 57σ for g_j and g_i with 6σ . These deviations differ largely also because the two g -factors are correlated fit parameters. The Zeeman model using g -factors as free fit parameters is again more accurate for the fit. This is indicated by the χ^2 value of 1.30 compared to 1.44 of the Landé g -factors. Also, the residuals are not randomly distributed for the Landé fit, as seen in figure 4.12b. The deviation of the Jefferies reference line is significant at -11σ .

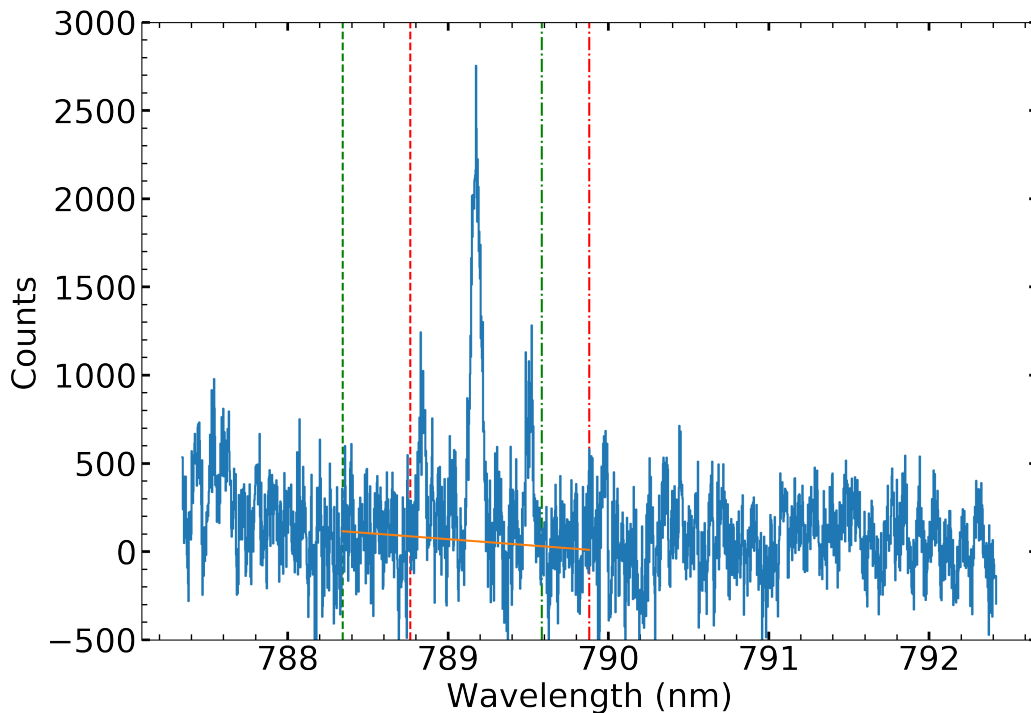
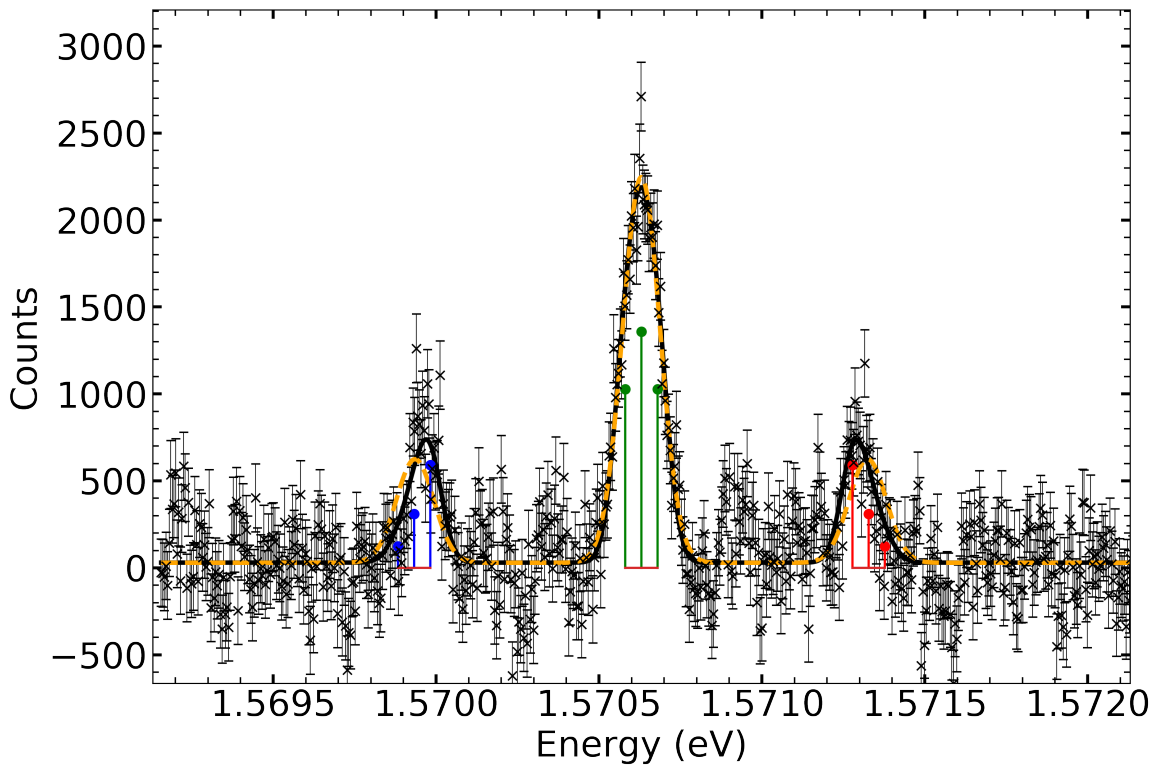
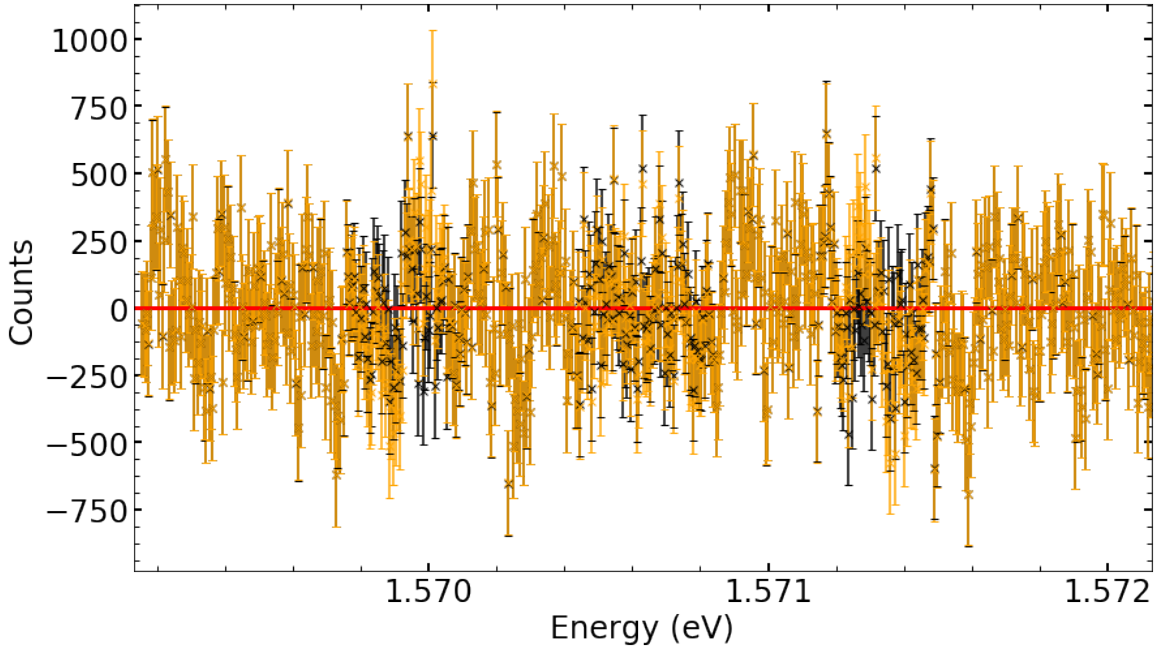


Figure 4.11 The linear baseline (orange) fitted in the two regions between the green and red lines. The blue line shows the whole range of the Fe spectrum after processing.



(a)



(b)

Figure 4.12 (a) Measurements of Fe^{10+} as black x with error bars. For this line, a linear baseline was subtracted from the data. For the black line, a Zeeman fit model was used with g -factors as fit parameters in comparison with the Zeeman model using Landé for fixed g -factors (orange, dashed). The coloured lines blue, green, red indicate the positions of the individual Zeeman components (using the free g -factors) with $\Delta m = -1$, $\Delta m = 0$, $\Delta m = +1$. (b) Residuals of the Zeeman fit with fixed g -factors (orange) and g -factors as fit parameters (black).

Table 4.15 Results of the Zeeman model fit in figure 4.12a

Property	<i>g</i> -factors fix	<i>g</i> -factors free
Line centre (nm)	789.3914(9)	789.3915(8)
Line centre (eV)	1.5706301(2)	1.5706301(2)
Line width (eV)	$5.75(2) \cdot 10^{-5}$	$3.76(4) \cdot 10^{-5}$
g_j initial	1.5	1.614(2)
g_j final	1.5	1.506(1)
offset (counts)	30(10) counts	30(10) counts
χ^2_{red}	1.44	1.30

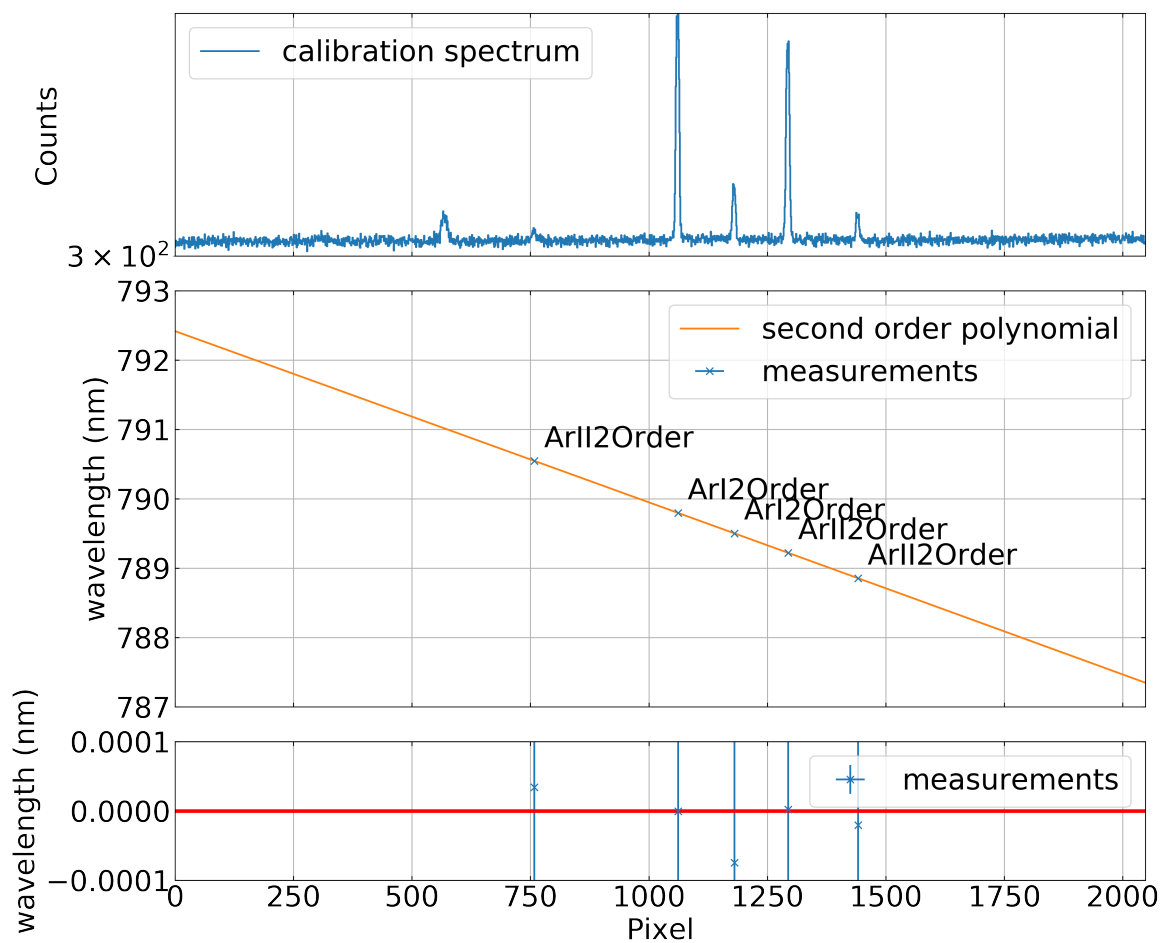
**Figure 4.13** Calibration Spectrum of the Fe-Ar lamp, fitted polynomial on the identified peaks, residuals of the fitted data points

Table 4.16 Calibration polynomial parameters

a (nm)	b (10^{-3} nm/pix)	c (10^{-9} nm/pix ²)	residual variance
792.41684(8)	-2.4619(1)	-6.6(1)	0.0034

The line at 569 pixel could not be identified with a NIST reference in first, second or third order. This line is also significantly wider than the other ones. The FWHMs are, in the order of the pixel positions, (14.1, 9.1, 7.5, 7.6, 7.9, 7.8) pixel. This indicates an overlap of multiple lines.

Table 4.17 Lines used for the calibration from NIST [41]. All the lines are in second order, in the original reference the wavelength is half of the listed wavelength.

peak (pixel)	wavelength (nm, air)	Ion	NIST reference
758.6	790.54560	Ar II second order	L11520 [47]
1061.62	789.7959	Ar I second order	L2634 [48]
1180.6	789.5010	Ar I second order	L2634 [48]
1294.29	789.21938	Ar II second order	L11520 [47]
1441.5	788.85424	Ar II second order	L11520 [47]

The uncertainties are, unlike the other lines, much larger for the Zeeman fit than for the calibration and indicates a precise calibration and a relatively inaccurate Zeeman fit due to the noisy signal.

$$\Delta\lambda_{\text{calibration}} = 1.6 \cdot 10^{-6} \text{ nm}$$

$$\Delta\lambda_{\text{Zeeman fit}} = 8.0 \cdot 10^{-4} \text{ nm}$$

$$\Delta\lambda_{\text{total}} = 8.0 \cdot 10^{-4} \text{ nm}$$

Table 4.18 Results compared to other works on this line. Using the values of the free g -factor. Equation 4.4 was used if the wavelength were given in air.

reference	wavelength (nm, vacuum)	
this work	789.3915(8)	
NIST: Jefferies 1971 [50]	789.40	solar eclipse observation

4.5.5 Fe¹⁴⁺ at 706 nm

The measurement of this line was unsuccessful. The spectral line which was assumed to be the Fe line, also appears in the calibration spectrum and the background measurement. The line positions are 197.25 pixel, 198.04 pixel and 199.26 pixel for these three spectra. It seems like the calibration lamp was not properly shielded from the spectrometer when performing the Fe and background measurement. The resulting wavelength for the assumed Fe line is 706.716(9) nm (air, Gaussian fit) where the NIST value is 705.86 nm (air) and an Ar I line is much closer at 706.7218 nm (air). In this context, it is assumed that the measured line was no Fe line but the calibration line only. Unexpected therefore is the Doppler broadening of the line comparing the Fe and the calibration spectrum. This results in a broadening of 0.0411(25) nm and a plausible ion cloud temperature of 31.8(2) eV.

4.6 Ion cloud temperature

The Doppler broadening of the Fe lines of the EBIT is related to the temperature of the ion cloud by the Maxwell distribution. This was derived in section 2.5.2. Equation 2.32 is used to calculate the ion cloud temperature in the EBIT by comparing the line width of the Doppler broadened Fe lines with lines of the much colder ions in the calibration lamp, where the Doppler shift is negligible.

$$T = \left(\frac{\Delta\lambda_D \cdot c}{\lambda_0} \right)^2 \cdot \frac{m}{8k_B \log 2} \quad (4.9)$$

With $\Delta\lambda_D = \sqrt{FWHM(Fe)^2 - FWHM(calibration)^2}$ is the Doppler broadening of the Fe line, m the Fe mass and k_B the Boltzmann constant [53, 54]. For the FWHM of the calibration line, a Gaussian fit was performed.

The temperature of the Fe¹²⁺ is about 8 eV larger for the 10 V deeper trapping potential (table 4.19). Evaporative cooling is enhanced for lower trapping potentials, thus induces a lower ion cloud temperature.

The Fe FWHM is largely determined by the Doppler broadening, where the Fe line width is roughly 1.5 (636 nm) - 3.5 (789 nm) of the calibration lines. The natural line width is many orders of magnitude smaller, e.g. for Fe¹³⁺ at 530 nm it is $9.4 \cdot 10^{-12}$ nm [7].

Note that for the 339 nm line the 3600/mm grating was used which leads to roughly half of the dispersion and the FWHM.

Table 4.19 Results for the ion could temperature.

line	FWHM Fe (nm)	FWHM Calibration (nm)	Doppler broadening (nm)	T (1000 K)	T (eV)
Fe ¹²⁺ at 339 nm and 435 V	0.0264(7)	0.0109(5)	0.0240(8)	547(1)	47.1(1)
Fe ¹²⁺ at 339 nm and 440 V	0.0241(5)	0.0109(5)	0.0215 (6)	437.0(7)	37.66(6)
Fe ¹³⁺ at 530 nm	0.0263(2)	0.0134(3)	0.0226(3)	198.05(6)	17.067(5)
Fe ⁹⁺ at 637 nm	0.0341(3)	0.0215(7)	0.0264(7)	182.6(3)	15.73(2)
Fe ¹⁰⁺ at 789 nm	0.045 (4)	0.0195(3)	0.040(4)	280(7)	24.1(6)

4.7 Polarisation

The Zeeman components have two perpendicular polarisations. In a perfect spectrometer, the relative intensities of these sub structural lines would only be given by the Clebsch-Gordan coefficients, but the spectrometers efficiency is dependent on the polarisation and the wavelength of the light. In the Zeeman fit the parameters A_0 and A_{\pm} model the spectrometer effect.

To quantify this dependency, for the new, in this work used, Mc Pherson and the older Triax 550 spectrometers, calibration lines of the Fe-Ar lamp were obtained for two perpendicular orientations of the wire grid polariser (section 3.2.4), which was placed directly in front of the spectrometer entrance slit. For wavelength from 200 nm to 700 nm, acquisitions of 30 seconds (Mc Pherson) and 5 seconds (Triax 550) were taken in steps of 20 nm. In each of the acquired spectra one Gaussian fit was performed for both polarisations of the same line, thus the ratio of integrals gives the relative intensities.

For the 339 nm line both relative intensities, for each trapping potential, are in a good agreement with the spectrometer polarisation dependency. The deviation increases with the wavelength for the (530, 637, 789) nm lines. However, the intensity ratio varies largely with increasing wavelength, thus an accurate prediction of the values between the measurements cannot be obtained. Because of that, especially the 789 nm lines deviation cannot be stated as large with a high certainty.

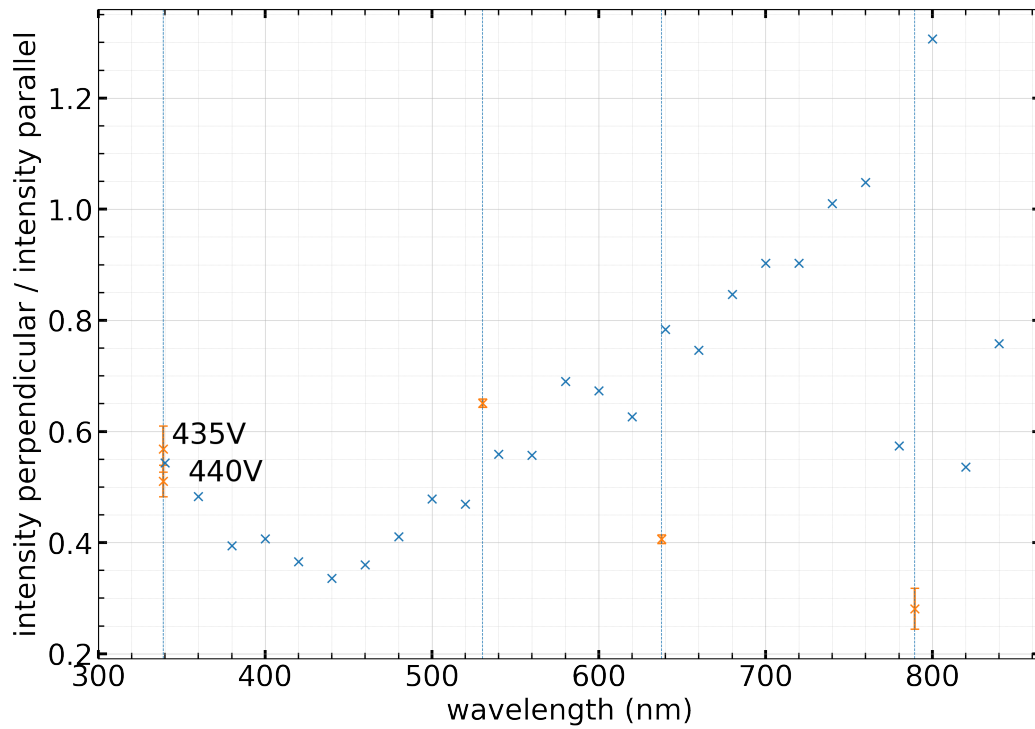


Figure 4.14 Intensity ratio of both polarisation orientations, for the calibration lamp lines of the Mc Person spectrometer (blue x) and for the Fe lines (orange x). The vertical blue dashed lines are plotted for orientation.

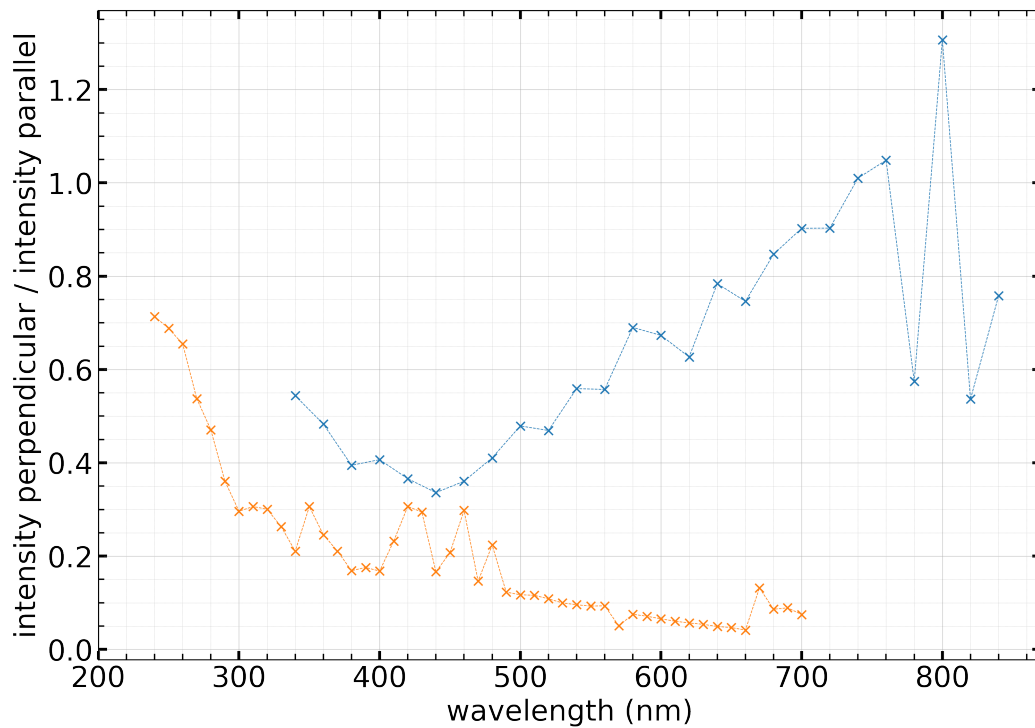


Figure 4.15 Intensity ratio of both polarisation orientations, for the calibration lines of the Mc Person spectrometer (blue x) and for the Triax 550 spectrometer (orange x)

Noticeable is that for the old spectrometer, using the same polariser and light source, spectral lines were observed also in a range of (240-340) nm, where the new spectrometer was not able to observe any lines. This is probably due to the wavelength dependent reflection properties of the aluminium plate which guides the calibration lamps light on the spectrometers optical path.

4.8 Magnetic field in the EBIT

The energy separation of the Zeeman components is given by equation 2.22, thus equally dependent on g -factors and magnetic flux. Instead of using the free g -factors, the magnetic flux B is determined as a free fit parameter while using the Landé g -factors. The calculations for the B -field in cases of wrong g -factors is not correct and therefore useless, which probably be the case for the two 339 nm lines. The plausibility of this analysis and the results are discussed in chapter 5.

Table 4.20 Magnetic flux in the EBIT

line	B (T)	Line centre (eV)	Line width (10^{-5} eV)	χ^2
Fe ¹³⁺ at 530 nm	7.944(5)	2.33743381(3)	4.920(4)	1.54
Fe ⁹⁺ at 637 nm	7.913(8)	1.94446069(4)	4.384(5)	2.56
Fe ¹²⁺ at 339 nm, 435 V	7.00(6)	3.6585069(5)	10.54(4)	11.23
Fe ¹²⁺ at 339 nm, 440 V	7.00(5)	3.6585060(3)	9.81(3)	7.88
Fe ¹⁰⁺ at 789 nm	7.67(5)	1.570630(2)	5.62(2)	1.32

4.9 Wavelength corrections of the solar observations

The highly charged Fe ions wavelengths of the NIST database, which are used for the comparison with the results of this work (table 5.1), were measured during solar eclipses. These observations are influenced by the Doppler effect of the moving plasma cloud around the sun. In the EBIT, the Doppler effect only affects the width of the line, as the ions velocities, positive and negative relative to the observer, are equally distributed. The ion cloud does not move as a whole. However, in the sun's corona, the velocities of the ions relative to the observer on the earth are not homogeneously distributed. This affects the wavelength measured on earth in multiple ways. The effects as well as the plausibility of this approximations are discussed in chapter 5.

4.9.1 Transversal Doppler Effect

The transversal movement of the ions from the surface of the sun, in the solar wind, is the cause of the transversal relativistic Doppler effect:

$$f'_{trans}/f = \sqrt{1 - \left(\frac{v}{c}\right)^2} \quad (4.10)$$

Where f'_{trans} is the shifted frequency, f the frequency in the ion's rest frame and v the transversal velocity of the ion. Assuming that the difference from the observed solar lines and the EBIT measurements is only due to this Doppler shift, the transversal ion velocity is approximated (table 4.21).

Table 4.21 Approximation of transversal velocities of the coronal Fe ions based on the EBIT measurements.

	solar observation (nm)	EBIT (nm)	v (10^6 m/s)
Edlen 1942	530.434	530.42870(8)	1.3
Jefferies 1971	637.64	637.6278(4)	1.9
Jefferies 1971	338.95	338.8930(3)	5.5
Jefferies 1971	789.40	789.3915(8)	1.4

4.9.2 Gravitational redshift

Another effect that shifts the wavelengths is the gravitational redshift due to the mass of the sun.

$$\lim_{r \rightarrow \infty} f'_r = f \sqrt{1 - \frac{r_s}{R_e}} \quad (4.11)$$

Where f'_r is the shifted frequency at the distance r from the centre of mass, R_e the distance of the centre of mass to the point of emission, and r_s the Schwarzschild radius:

$$r_s = \frac{2GM}{c^2} \quad (4.12)$$

with the Newtons gravitational constant G and the mass M , in this case of the sun [55]. For this rough estimation, $R_e = 10^6$ m was chosen since the solar radius is (696342 ± 65) km [56] but the corona is millions of kilometres thick. Thus, this estimate considers ions relatively close to the photosphere of the sun and therefore leads to a rather large effect.

Table 4.22 Approximation of gravitational redshift of the coronal Fe ions using the wavelength of this work.

EBIT measurement (nm)	$\Delta\lambda$ (pm)
530.42870(8)	0.8
637.6278(4)	0.9
338.8930(3)	0.5
789.3915(8)	1.2

Chapter 5

Discussion

In this work, multiple wavelengths of Fe transitions were obtained with high precision, the results being summarised in table 5.1. For all the determined wavelengths, the uncertainties are between 5 and 13.5 times smaller than those of the previous best measurement. The Fe¹³⁺ at 530 nm and the Fe⁹⁺ at 637 nm lines are very well resolved, since the counts between two Zeeman components are on background level. However, the line at 789 nm is relatively noisy and less intense than the other lines, what caused a relatively large Zeeman fit uncertainty (table 5.2). The relative uncertainties (uncertainty/value) are $1.5 \cdot 10^{-7}$ (530 nm), $6.3 \cdot 10^{-7}$ (637 nm), $1.2 \cdot 10^{-6}$ (339 nm), $1.0 \cdot 10^{-6}$ (789 nm), thus very small.

The Zeeman fitting model with g -factors as fit parameters is a suitable model for all the measured lines, certainly more appropriate than the fitting using Landé g -factors. This is indicated by χ^2 values and residual distributions of all measured lines.

The ion cloud temperature (section 4.6), is relatively low and achieved using evaporative cooling, ranged from 16.09 eV to 47.1 eV. However, the Doppler broadening is the largest contribution to the line width (table 4.19). The influence of evaporative cooling was directly observed for the two trapping potentials in the 339 nm sequence.

In the Fe⁹⁺ at 637 nm and Fe¹²⁺ at 339 nm cases, the calibration determines the total uncertainty (table 5.2). For the Fe¹³⁺ at 530 nm, the Zeeman fit uncertainty is about 4 times, and for the Fe¹⁰⁺ at 789 nm line about 500 times, of the calibration uncertainty. Nevertheless, for all lines, except for the 789 nm one, the calibration error is of the same order of magnitude as the Zeeman fit uncertainty, and does not increase the order of magnitude in the total uncertainty.

Table 5.1 All results compared to other works on the lines including deviations and possible reasons for these deviations.

this work (nm, vacuum)	reference (nm, vacuum)	reference	deviation σ	deviation (pm)	transversal Doppler shift for $v = 750$ km/s (pm)	gravitational red shift (pm)
530.42870(8)	530.4276(4)	Schnorr 2013, 2011 [7, 23] EBIT laser spectroscopy	14	1.1		
	530.4228(1)	Link 2010 [27] EBIT spectroscopy	74	5.9		
	530.423(8)	Arnesh 2014 [44] EBIT spectroscopy	71	5.7		
	530.4240(5)	Rybanský 1986 [45] solar eclipse observation	59	4.7		
	530.434	NIST: Edlen 1942 [46] solar eclipse observation	-66	-5.3	-1.7	-0.8
637.6277(4)	637.630(1)	Brenner 2009 [49] EBIT spectroscopy	-23	-2.3		
	637.64	NIST: Jefferies 1971 [50] solar eclipse observation	-123	-12.3	-2.0	-0.9
	637.627	NIST: Grotian 1939 [5] solar eclipse observation	-	-	-	-
338.8930(3)	338.885(3)	Arnesh 2014[44] EBIT spectroscopy	26	8		
	338.95	NIST: Jefferies 1971 [50] solar eclipse observation	-190	-5.7	-1.1	-0.5
	338.91	NIST: Huang 1985 [52] E2, Dirac-Fock calculation	-57	-17		
789.3915(8)	789.40	NIST: Jefferies 1971 [50] solar eclipse observation	-11	-8.5	-2.5	-1.2

The calibration uncertainty could possibly be improved by identifying more suitable spectral lines for the calibration. Since the values from NIST do not specify any uncertainty, it was estimated to be ± 1 on the last digit. This is a small estimate, which leads to a large estimate of the fit parameter's uncertainty, but a small estimate for the calibration uncertainty of the line, because it was determined using a confidence band. The residuals of the calibration polynomial show deviations that would be within the error bars of a larger error estimation.

Table 5.2 Uncertainties of the measured Fe lines

line	$\Delta\lambda_{\text{calibration}}$ (nm)	$\Delta\lambda_{\text{Zeeman fit}}$ (nm)	$\Delta\lambda_{\text{total}}$ (nm)
Fe ¹³⁺ at 530 nm	$1.8 \cdot 10^{-5}$	$7.7 \cdot 10^{-5}$	$7.9 \cdot 10^{-5}$
Fe ⁹⁺ at 637 nm	$4.2 \cdot 10^{-4}$	$1.4 \cdot 10^{-4}$	$4.4 \cdot 10^{-4}$
Fe ¹²⁺ at 339 nm (435 V/ 440 V)	$4.2 \cdot 10^{-4}/$ $4.0 \cdot 10^{-4}$	$2.2 \cdot 10^{-4}/$ $1.9 \cdot 10^{-4}$	$4.8 \cdot 10^{-4}/$ $4.4 \cdot 10^{-4}$ both $3.3 \cdot 10^{-4}$
Fe ¹⁰⁺ at 789 nm	$1.6 \cdot 10^{-6}$	$8.0 \cdot 10^{-4}$	$8.0 \cdot 10^{-4}$

In Table 5.1, the deviations of the solar observations are listed. Almost all of them have larger wavelength than the EBIT measurements, the lines are red shifted by the Doppler effect and the gravitational redshift. Only the measurement of Rybanský has a shorter wavelength, but it is not clear if the Doppler effect was already considered, since very little information on the measurements is given in the original work [45]. In this work, several effects need to be considered. The relativistic transversal Doppler shift of the ions moving perpendicular to the solar surface, in the plane parallel to the observation plane, is calculated in section 4.9.1. Based on the assumption that this effect is the only source of the deviation, the transversal velocities are calculated at $(1.3, 1.9, 5.5, 1.4) \cdot 10^6$ m/s, which is not in a plausible range. Typical values for the traversal coronal velocities are 300-500 km/s for slow and 750 km/s for fast solar winds [57]. Coronal mass ejections lead to velocities of up to 2000 km/s [58], but are not likely to have this large influence on the measurements. In table 5.1 the wavelength shifts are stated for the high but common velocity of 750 km/s. When comparing that values with the ones deviations, it is clear that the deviation of this EBIT measurement and the corona observation cannot be explained by the relativistic transversal Doppler shift alone.

The gravitational red shift also affects the wavelength (section 4.9.2). A rough estimation of this effect is also stated in table 5.1.

The ions also move in the longitudinal direction and shift the wavelengths by another Doppler effect. Even when during a solar eclipse the observational region is a disc, with the sun covered, some ions move longitudinal towards the observer. This effect may result in large shifts of the solar observations, but the approximation of this Doppler effect is an advanced astrophysical task, since detailed information about the velocities and number of ions moving in this direction is needed.

For the two 339 nm lines, the g -factors determined in the Zeeman fit deviate largely from the Landé g -factors (table 5.3). The Landé g -factors are more precise than this result suggests, relativistic corrections assumed to be in the per mill range, QED and other effects even smaller. The fit results of the g -factors are correlated with the width of the Zeeman lines and the magnetic field in the trap. The magnetic flux of 8 T in the centre of the trap is known from the design of the two superconducting Helmholtz coils. The computed magnetic field data is available from the manufacturer. The magnetic flux in the trapping region differs at most with about one per mille from 8 T, not causing such deviations. Also, the reducing current in the coils, due to non-perfect superconducting properties, is no sufficient explanation for these large deviations. The widths are in a reasonable range, compared to the other values in this work (table 4.19). Possibly, the g -factors are not matching because the transition was wrongly identified. The identification of another transition is an advanced task not done in this work.

The g -factors in the Fe^{12+} at 339 nm line may be affected by the admixture of the also possible yet not considered E2 transition and the previously stated M1 transitions. The occurrence of the two transitions possibly causes an interference effect of this transition, similar to the effect stated in the work of Werbowy and Kwela in 2008 for Bi I [59].

The values of the magnetic field B vary largely (table 4.20) in the same way the g -factors deviate from the Landé g -factors (table 5.3), because both factors are strongly correlated. In this sense, the calculations for the B -field in cases of wrong g -factors, is wrong and useless. For the 789 nm line, also the magnetic field B and the g -factors deviate largely from the expected values, but this is probably caused by the noisy measurements resulting in an imprecise fit.

The Fe^{13+} at 530 nm line was already measured in the same EBIT, compared to these older measurements in figure 5.1a and 5.1b, this work is much better resolved (figure 4.4a). This is due to the new spectrometer, which has eight times larger linear dispersion [60]. The σ

Table 5.3 g -factors calculated using the Landé equation compared to the g -factors determined as fit parameters and the deviations of those two values.

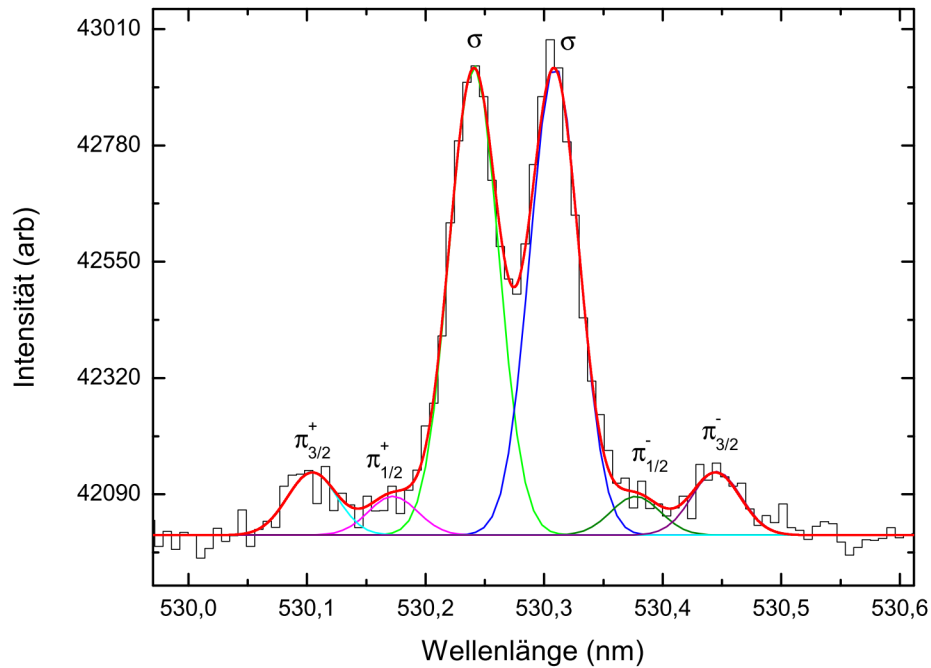
line	Landé:			Fit:			Landé:			Fit:			
	g_i	absolute	%	g_i	absolute	%	g_f	absolute	%	g_f	absolute	%	σ
530 nm	4/3	-0.0105	-0.79	1.3228(1)	-0.0105	-0.79	2/3	-0.0084	-1.26	0.6583(3)	-0.0084	-1.26	-28
637 nm	2/3	-0.0126	-1.89	0.6541(3)	-0.0126	-1.89	4/3	-0.0166	-1.25	1.3167(2)	-0.0166	-1.25	-84
339 nm, 435 V	1	+0.035	+3.5	1.035(3)	+0.035	+3.5	3/2	-0.05	-3.33	1.450(3)	-0.05	-3.33	-17
339 nm, 440 V	1	+0.080	+8	1.080(3)	+0.080	+8	3/2	-0.008	-0.53	1.492(2)	-0.008	-0.53	-4
789 nm	3/2	+0.114	+7.60	1.614(2)	+0.114	+7.60	3/2	+0.006	+0.4	1.506(1)	+0.006	+0.4	+6

polarised components are not visible in the measurements of Schnorr 5.1b because the observation axis was parallel to the magnetic field. The intensity relations of the lines components are very different for the Link measurement (figure 5.1a) compared to this work (figure 4.4a). This difference is in good agreement with the measured polarisation properties of the two used spectrometers (section 4.7).

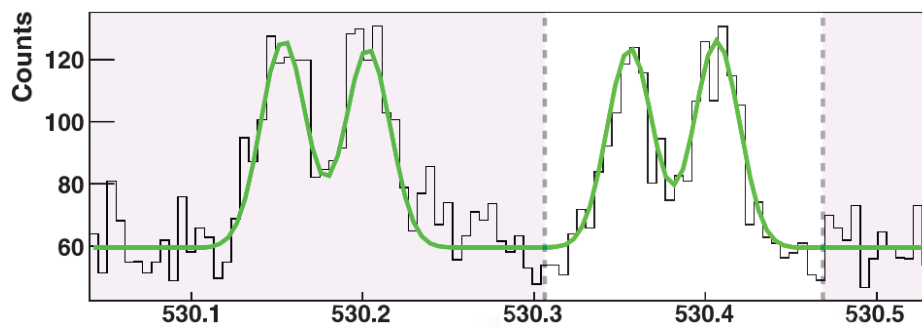
Possible variations of the background, for example due to temperature changes, could not be compensated because the background images were taken only at the end of the whole sequence. In figure 5.2a the mean of all pixels is plotted against the acquisitions number. The sequence for the 789 nm acquisition does not show any significant trend. The mean counts increase for the 339 nm (440 V) and the 637 nm line by about 1 count. The change in the mean counts for the 339 nm (435 V) sequence is significant, what led to the correction of the trapping potential. In the Fe^{13+} at 530 nm line, a large variation of the average intensity, in the course of all acquisitions is visualised in figures 5.2a, 5.2b. This might be caused by the pressure reduction of the, at this time just attached, $\text{Fe}(\text{CO})_5$ bottle. Inaccurate background measurements lead to more noise in the measured data. This could be avoided by acquiring more background measurements, e.g. every 10-15 Fe acquisitions. Not too loose too many Fe counts, it is possible to do 10-15 minute background images and extrapolate them to 30 minutes.

The polarisation properties of the spectrometer, determined in measurement with a polarisation filter and as a factor in the Zeeman fit, deviate largely (figure 4.14). The diffuse aluminium reflector that guides the light from the calibration lamp to the spectrometer setup, affects the polarizations and is not used for the EBIT light. This might explain the large deviations of the polarisation ratios. The spectrometer measurements would have been much better comparable to the Fe line results if the Fe wavelengths previously obtained had been used for the spectrometer measurement. Because the spectrometer measurement were not calibrated, second order transitions could not be avoided and might explain the large variations especially in the larger wavelength region because it is more likely for these wavelengths (figure 4.14).

Nevertheless, the wavelengths obtained in this work are the most precise values of the Fe lines measured up today. The resolution of the Zeeman splitting leads to yet unclear processes which cause the large deviation of the g -factors in the Fe^{12+} at 339 nm lines. These results need to be further evaluated, which may lead to new insights of the admixture of M1-E2 transitions.

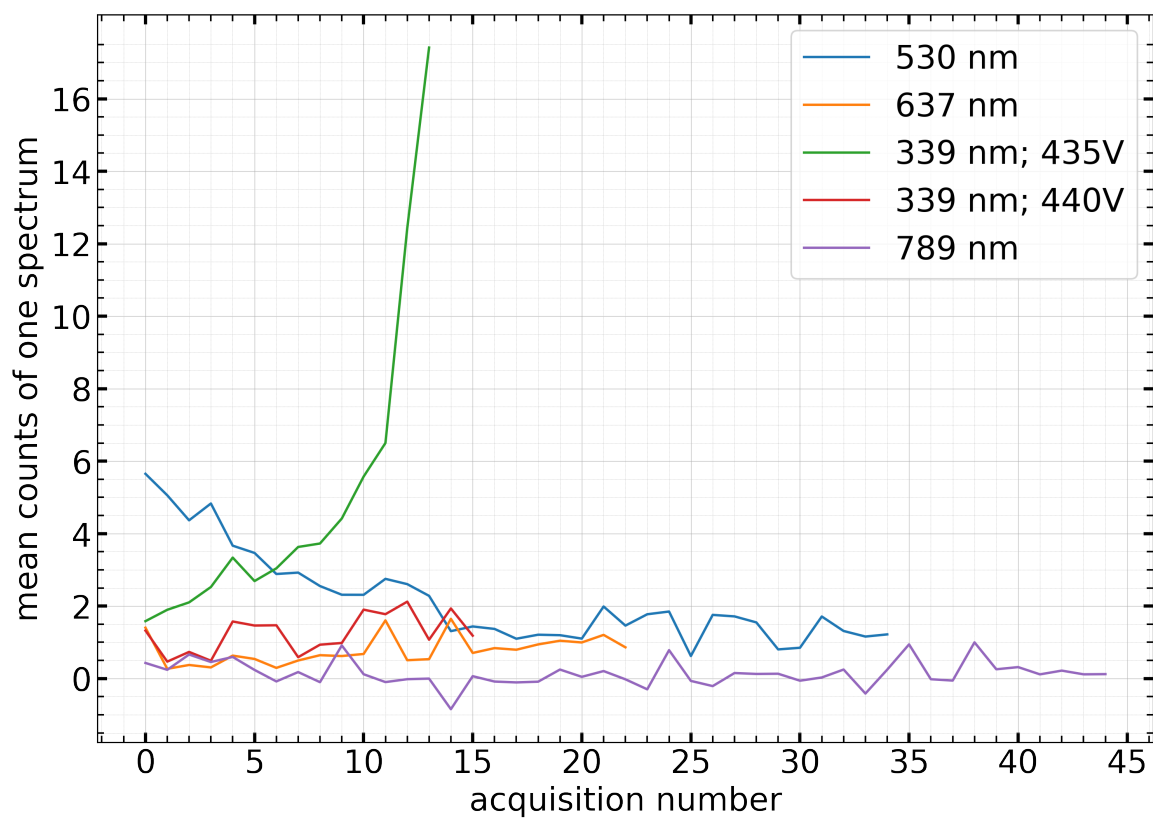


(a)

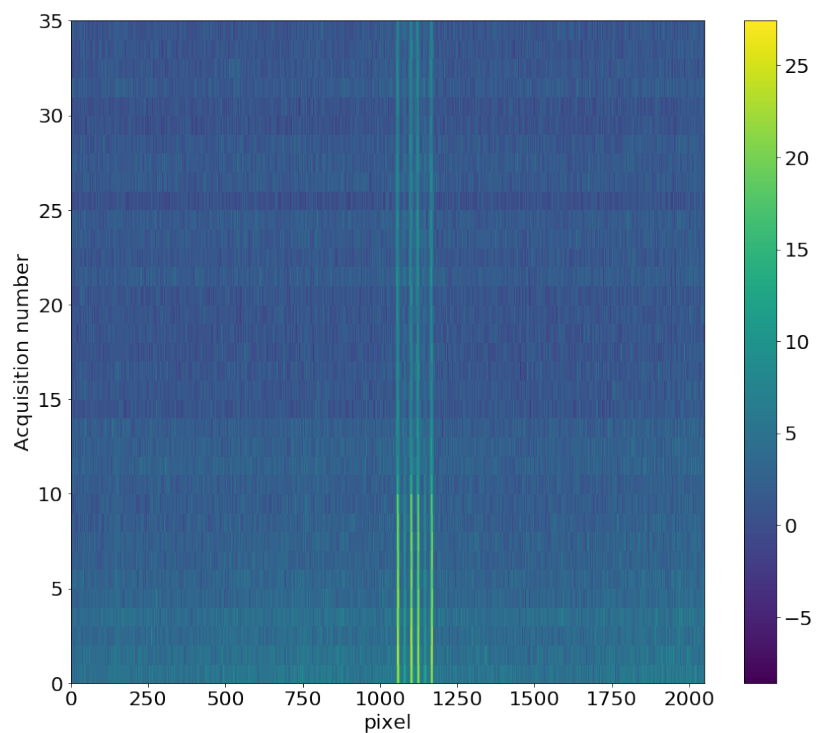


(b)

Figure 5.1 (a) Measurements of Fe^{13+} at 530.4228(1) nm by Julia Link in 2010 [27] (b) Measurements of Fe^{13+} at 530.4276(4) nm by Kirsten Schnorr in 2013 [7]. Both wavelength axes are in air but the given wavelengths are in vacuum.



(a)



(b)

Figure 5.2 (a) Mean counts of all pixel in one spectrum after processing against the acquisition number. (b) Fe^{13+} at 530 nm. The colour bar visualises the counts after processing.

Acknowledgements

First, I thank José Ramón Crespo López-Urrutia for trusting me with this work, advising me with his vast knowledge and inspiring me with his unstoppable passion.

I thank Hendrik Bekker for giving me the opportunity to work alongside him, as well as his patient and intense dedication to the supervision of this work. I also thank him for the very valuable proofreading and all the little and big lessons on physics and technology.

I thank all the EBIT team at MPIK for the support and all the nice coffee break talks.

I want to thank Alba Gordó i Vilaseca, for her very valuable and discerning proofreading and support.

To end up with, none of this would have been possible without the unconditional support of my parents and brother, nor without their constant encouragement.

Bibliography

- [1] Isaac Newton. Opticks: Or, a treatise of the reflexions, refractions, inflexions and colours of light. *The Royal British Society*, 1:416, 1704. ISSN 1098-6596. doi: 10.1007/s13398-014-0173-7.2.
- [2] Joseph Fraunhofer. Bestimmung des Brechungs- und des Farbenzerstreungs-Vermögens verschiedener Glasarten, in Bezug auf die Vervollkommnung achromatischer Fernröhre. *Annalen der Physik*, 56(7):264–313, jan 1817. ISSN 15213889. doi: 10.1002/andp.18170560706. URL <http://doi.wiley.com/10.1002/andp.18170560706>.
- [3] G. Kirchhoff and R. Bunsen. Chemische Analyse durch Spectralbeobachtungen. *Annalen der Physik und Chemie*, 186(6):161–189, jan 1860. doi: 10.1002/andp.18601860602. URL <http://doi.wiley.com/10.1002/andp.18601860602>.
- [4] Charles Augustus Young. *The Sun and the phenomena of its atmosphere*, volume 8. CC Chatfield, 1872. ISBN 3663537137. doi: 10.1016/0003-6870(73)90259-7.
- [5] W. Grotian. Zur Frage der Deutung der Linien im Spektrum der Sonnenkorona. *Die Naturwissenschaften*, 27(13):214, 1939. ISSN 00281042. doi: 10.1007/BF01488890.
- [6] J W Cirtain, L Golub, A R Winebarger, B De Pontieu, K Kobayashi, R L Moore, R W Walsh, K E Korreck, M Weber, P McCauley, A Title, S Kuzin, and C E DeForest. Energy release in the solar corona from spatially resolved magnetic braids. *Nature*, 493(7433):501–503, 2013. ISSN 1476-4687. doi: 10.1038/nature11772. URL <http://dx.doi.org/10.1038/nature11772>.
- [7] K. Schnorr, V. Mäckel, N. S. Oreshkina, S. Augustin, F. Brunner, Z. Harman, C. H. Keitel, J. Ullrich, and J. R. Crespo López-Urrutia. Coronium in the laboratory: measuring the Fe XIV Grenn Coronal Line by Laser Spectroscopy. *The Astrophysical Journal*, 776(2):121, 2013. ISSN 0004-637X. doi: 10.1088/0004-637X/776/2/121. URL <http://iopscience.iop.org/0004-637X/776/2/121/article/>.
- [8] S. Rifai Habbal, M. Druckmüller, H. Morgan, I. Scholl, V. Rušin, A. Daw, J. Johnson, and M. Arndt. Total Solar Eclipse Observations of Hot Prominence Shrouds. *The Astrophysical Journal*, 719(2):1362–1369, aug 2010. ISSN 0004-637X. doi: 10.1088/0004-637X/719/2/1362. URL <http://stacks.iop.org/0004-637X/719/i=2/a=1362?key=crossref.8f2748fc791c7661d1ab453824136d2b>.
- [9] Steven B. Kraemer and D. Michael Crenshaw. Resolved Spectroscopy of the Narrow-Line Region in NGC 1068. II. Physical Conditions near the NGC 1068 “Hot Spot”. *The*

- Astrophysical Journal*, 532(1):256–266, mar 2000. ISSN 0004-637X. doi: 10.1086/308572. URL <http://stacks.iop.org/0004-637X/532/i=1/a=256>.
- [10] B. E. Woodgate, Jr. Stockman, H. S., J. R. P. Angel, and R. P. Kirshner. Detection of the [Fe XIV] Coronal Line at 5303 Å in the Cygnus Loop. *The Astrophysical Journal*, 188:L79, mar 1974. ISSN 0004-637X. doi: 10.1086/181438. URL <http://adsabs.harvard.edu/doi/10.1086/181438>.
- [11] J. H. M. M. Schmitt and R. Wichmann. Ground-based observation of emission lines from the corona of a red-dwarf star. *Nature*, 412(6846):508–510, aug 2001. ISSN 0028-0836. doi: 10.1038/35087513. URL <http://www.nature.com/doi/10.1038/35087513>.
- [12] V. A. R. M. Ribeiro, M. F. Bode, M. J. Darnley, D. J. Harman, A. M. Newsam, T. J. O'Brien, J. Bohigas, J. M. Echevarría, H. E. Bond, V. H. Chavushyan, R. Costero, R. Coziol, A. Evans, S. P. S. Eyres, J. León-Tavares, M. G. Richer, G. Tovmassian, S. Starrfield, and S. V. Zharikov. The Expanding Nebular Remnant of the Recurrent Nova Rs Ophiuchi (2006). ii. Modeling of Combined Hubble Space Telescope Imaging and Ground-Based Spectroscopy. *The Astrophysical Journal*, 703(2):1955–1963, oct 2009. ISSN 0004-637X. doi: 10.1088/0004-637X/703/2/1955. URL <http://iopscience.iop.org/0004-637X/703/2/1955><http://stacks.iop.org/0004-637X/703/i=2/a=1955?key=crossref.24bdda72f56e19247011f1295d08dace>.
- [13] Hermann Haken and Hans Christoph Wolf. *Atom - und Quantenphysik*. Springer-Verlag Berlin Heidelberg GmbH, 8 edition, 2004. ISBN 9783642621420.
- [14] G.E. Uhlenbeck and S. Goudsmit. Ersetzung der Hypothese vom unmechanischen Zwang durch eine forderung bezüglich des innern Verhaltens jedes einzelnen Elektrons. *Die Naturwissenschaften*, 13(47):953–954, 1925.
- [15] Walther Gerlach and Otto Stern. Der experimentelle Nachweis der Richtungsquantelung im Magnetfeld. *Zeitschrift für Physik*, 9(1):349–352, 1922. ISSN 14346001. doi: 10.1007/BF01326983.
- [16] Christopher J. Foot. *Atomic Physics*. Oxford University Press, 2005. ISBN 0 19 850695 3. doi: 10.1038/466035a.
- [17] P. a. M. Dirac. The Quantum Theory of the Emission and Absorption of Radiation. *Proceedings of the Royal Society A: Mathematical, Physical and Engineering Sciences*, 114(767):243–265, 1927. ISSN 1364-5021. doi: 10.1098/rspa.1927.0039. URL <http://www.ncbi.nlm.nih.gov/htbin-post/Entrez/query?db=m{&}form=6{&}dopt=r{&}uid=8097327>.
- [18] Jay Orear. *Nuclear physics : a course given by Enrico Fermi at the University of Chicago*. University of Chicago Press, Chicago, 1974. ISBN 9780226243658.
- [19] Franz Schwabl. *Quantenmechanik (QM I)*. Springer-Verlag Berlin Heidelberg, 7. auflage edition, 2007. ISBN 978-3-540-73674-5. doi: 10.1007/978-3-540-73675-2.
- [20] Gordon W. F. Drake, editor. *Springer handbook of atomic, molecular, and optical physics*. Springer, New York, NY, 2006. ISBN 0-387-20802-X and 978-0-387-20802-2.

- [21] *Fortgeschrittenen Praktikum: Zeeman effect*. Max-Planck-Institut für Kernphysik, 2012.
- [22] Wolfgang Demtröder. *Experimentalphysik 3*, volume 5. Springer-Verlag Berlin Heidelberg, 5 edition, 2016.
- [23] Kirsten Schnorr. Laserspektroskopie hochgeladener Ionen an einer EBIT, 2011.
- [24] Michael A Blessohl. Optische Spektroskopie an hochgeladenen Bismut-Ionen und Konstruktion eines hochauflösenden VUV-Gitterspektrometers, 2015.
- [25] Antonio Javier Gonzalez Martinez. *Quantum interference in the dielectric recombination of heavy highly charged ions*. PhD thesis, Ruperto-Carola University of Heidelberg, 2005.
- [26] Kirsten Schnorr and Volkhard Mäkel. Fe13plus grüne Linie in der Ebit, 2010.
- [27] Julia Link. Hochgenaue Laborbestimmung der Wellenlänge des verbotenen Übergangs der FeXIV-Linie, 2010.
- [28] Hendrik Bekker. *Optical and EUV spectroscopy of highly charged ions near the 4f–5s level crossing*. PhD thesis, Ruperto-Carola-University of Heidelberg, Germany, 2016.
- [29] Alexander Windberger. *Identification of optical transitions in complex highly charged ions for applications in metrology and tests of fundamental constants*. PhD thesis, Ruperto-Carola-University of Heidelberg, Germany, 2015.
- [30] Renee Klawitter. Resonant laser spectroscopy of a visible magnetic dipole transition in Ar13+, 2009.
- [31] M Czerny and A.F. Turner. Über den Astigmatismus bei Spiegelspektrometern. *Zeitschrift für Physik*, 61(11):792–797, 1930. doi: 10.1007/BF01340206. URL <https://doi.org/10.1007/BF01340206>.
- [32] FeuRenard. Czerny-Turner monochromator, 2014. URL <https://commons.wikimedia.org/w/index.php?curid=9934696>.
- [33] Vigneshdm. Diffraction Grating Equation, 1990. URL <https://commons.wikimedia.org/w/index.php?curid=58383485>.
- [34] Andor Technology. System Performance, 2016.
- [35] Bob Mellish. Wire-grid-polarizer, 2006. URL <https://commons.wikimedia.org/wiki/File:Wire-grid-polarizer.svg>.
- [36] Thorlabs. Thorlabs - WP25M-UB Ø25.0 mm Mounted Wire Grid Polarizer, 250 nm to 4 µm, 2017. URL <https://www.thorlabs.com/thorproduct.cfm?partnumber=WP25M-UB>.
- [37] J. Scofield. Ionization Energies, 1975.
- [38] Wojtek Pych. A Fast Algorithm for Cosmic Rays Removal from Single Images, nov 2003. URL <http://arxiv.org/abs/astro-ph/0311290><http://dx.doi.org/10.1086/381786>.

- [39] Peter J. Mohr, David B. Newell, and Barry N. Taylor. CODATA Recommended Values of the Fundamental Physical Constants: 2014, jul 2015. URL <http://arxiv.org/abs/1507.07956><http://dx.doi.org/10.1103/RevModPhys.88.035009>.
- [40] Edison Peck and Kaye Reeder. Dispersion of Air. *Journal of the Optical Society of America*, 62(8):958–962, 1972. ISSN 0030-3941. doi: 10.1364/JOSA.62.000958. URL <http://www.opticsinfobase.org/abstract.cfm?URI=josa-62-8-958>.
- [41] A. Kramida, Yu. Ralchenko, J. Reader, and NIST ASD Team. NIST Atomic Spectra Database (ver. 5.3), [Online]. Available: <http://physics.nist.gov/asd> [2017, July 27]. National Institute of Standards and Technology, Gaithersburg, MD., 2015.
- [42] James C. Ehrhardt and Sumner P. Davis. Precision Wavelengths and Energy Levels in Gold. *Journal of the Optical Society of America*, 61(10):1342, 1971. ISSN 0030-3941. doi: 10.1364/JOSA.61.001342.
- [43] Keivin Burns, Kenneth B Adams, and Jean Longwell. Interference Measurements in the Spectra of Neon and Natural Mercury. *Journal of the Optical Society of America*, 40(1925):339, 1950. ISSN 0030-3941. doi: 10.1364/JOSA.40.000339. URL <https://www.osapublishing.org/abstract.cfm?URI=josa-40-6-339>.
- [44] John Arnesh Divakaruni Daniel. Optical Spectroscopy of Highly Charged Iron Ions, 2014.
- [45] M. Rybanský, V. Rušin, and G. Dermendjiev, V.; Buyukliyev. On the wavelength of the green coronal line - Fe XIV. *Contributions of the Astronomical Observatory Skalnaté Pleso*, 15:p.419, 1986. URL <http://adsabs.harvard.edu/abs/1986CoSka..15..419R>.
- [46] B Edlen. Die Deutung der Emissionslinien im Spektrum der Sonnenkorona. *Zeitschrift für Astrophysik*, 22, 1942. ISSN 0717-6163. doi: 10.1007/s13398-014-0173-7.2.
- [47] W. Whaling, W.H.C. H C Anderson, M.T. T. Carle, J.W. W. Brault, and H.A. A. Zarem. Argon ion linelist and level energies in the hollow-cathode discharge. *Journal of Quantitative Spectroscopy and Radiative Transfer*, 53(1):1–22, jan 1995. ISSN 00224073. doi: 10.1016/0022-4073(94)00102-D. URL <http://linkinghub.elsevier.com/retrieve/pii/002240739400102D>.
- [48] Göran Goran Norlén. Wavelengths and Energy Levels of Ar I and Ar II Based on New Interferometric Measurements in the Region 3 400 - 9 800 Å. *Physica Scripta*, 8(6):249–268, dec 1973. ISSN 0031-8949. doi: 10.1088/0031-8949/8/6/007. URL <http://stacks.iop.org/1402-4896/8/i=6/a=007?key=crossref.f35f5eff9e2bab783899983ce36b2c13>.
- [49] G. Brenner, J. R. Crespo López-Urrutia, S. Bernitt, D. Fischer, R. Ginzl, K. Kubiček, V. Mäckel, P. H. Mokler, M. C. Simon, and J. Ullrich. ON THE TRANSITION RATE OF THE Fe X RED CORONAL LINE. *The Astrophysical Journal*, 703(1):68–73, 2009. ISSN 0004-637X. doi: 10.1088/0004-637X/703/1/68. URL <http://stacks.iop.org/0004-637X/703/i=1/a=68?key=crossref.895ddd0579cb6d7c1c7132b863329ac>.
- [50] John T. Jefferies, Frank Q. Orrall, and J. B. Zirker. The spectrum of the inner corona observed during the total solar eclipse of 30 May 1965. *Solar Physics*, 16(1):103–110, 1971. ISSN 00380938. doi: 10.1007/BF00154505.

- [51] A. E. Kramida and G. Nave. The Ne II spectrum. *European Physical Journal D*, 39(3): 331–350, 2006. ISSN 14346060. doi: 10.1140/epjd/e2006-00121-4.
- [52] Keh-Ning Huang. Energy-level scheme and transition probabilities of si-like ions. *Atomic Data and Nuclear Data Tables*, 32(3):503 – 566, 1985. ISSN 0092-640X. doi: [http://dx.doi.org/10.1016/0092-640X\(85\)90022-1](http://dx.doi.org/10.1016/0092-640X(85)90022-1). URL <http://www.sciencedirect.com/science/article/pii/0092640X85900221>.
- [53] Peter Mohr, Barry Taylor, and David Newell. CODATA recommended values of the fundamental physical constants: 2010. *Reviews of Modern Physics*, 84(4):1527–1605, 2012. ISSN 0034-6861. doi: 10.1103/RevModPhys.84.1527. URL <http://link.aps.org/doi/10.1103/RevModPhys.84.1527>.
- [54] Juris Meija, Tyler B. Coplen, Michael Berglund, Willi A. Brand, Paul De Bièvre, Manfred Gröning, Norman E. Holden, Johanna Irrgeher, Robert D. Loss, Thomas Walczyk, and Thomas Prohaska. Atomic weights of the elements 2013 (IUPAC Technical Report). *Pure and Applied Chemistry*, 88(3):265–291, 2016. ISSN 13653075. doi: 10.1515/pac-2015-0305.
- [55] William M Folkner, James G Williams, Dale H Boggs, W M Folkner, E M Standish, J G Williams, and D H Boggs. The Planetary and Lunar Ephemeris DE 421, 2009. URL https://ipnpr.jpl.nasa.gov/progress/_report/42-178/178C.pdf.
- [56] Marcelo Emilio, Jeff R Kuhn, Rock I Bush, and Isabelle F Scholl. Measuring the Solar Radius from Space during the 2003 and 2006 Mercury Transits. *The Astrophysical Journal*, 750(8pp), 2012. ISSN 0004-637X. doi: 10.1088/0004-637X/750/2/135. URL <http://iopscience.iop.org/article/10.1088/0004-637X/750/2/135/pdf><http://arxiv.org/abs/1203.4898>{%}0A<http://dx.doi.org/10.1088/0004-637X/750/2/135>.
- [57] J. Geiss, G. Gloeckler, and R. von Steiger. Origin of the Solar Wind from Coposition Data. *Space Science Reviews*, 72:49–60, 1995. ISSN 0038-6308. doi: 10.1007/BF00768753.
- [58] O. C. St. Cyr, R. a. Howard, N. R. Sheeley, S. P. Plunkett, D. J. Michels, S. E. Paswaters, M. J. Koomen, G. M. Simnett, B. J. Thompson, J. B. Gurman, R. Schwenn, D. F. Webb, E. Hildner, and P. L. Lamy. Properties of coronal mass ejections: SOHO LASCO observations from January 1996 to June 1998. *Journal of Geophysical Research*, 105 (A8):18169, 2000. ISSN 0148-0227. doi: 10.1029/1999JA000381.
- [59] S Werbowy and J Kwela. M1-E2 interference in the Zeeman spectra of BiI. *Physical Review A - Atomic, Molecular, and Optical Physics*, 77(2), 2008. ISSN 10502947. doi: 10.1103/PhysRevA.77.023410. URL <https://journals.aps.org/prapdf/10.1103/PhysRevA.77.023410>.
- [60] Julian Rauch. Montage und Charakterisierung eines hochauflösenden optischen Spektrometers zur Vermessung verbotener optischer Übergänge in hochgeladenen Ionen an der Heidelberger Elektronenstrahl-Ionenfalle, 2017.

Erklärung

Ich versichere, dass ich diese Arbeit selbstständig verfasst und keine anderen als die angegebenen Quellen und Hilfsmittel benutzt habe.

Heidelberg, den ...,